© 2023. Published by The Company of Biologists Ltd | Journal of Cell Science (2023) 136, jcs260159. doi:10.1242/jcs.260159

RESEARCH ARTICLE

Toxoplasma gondii scavenges mammalian host organelles through the usurpation of host ESCRT-III and Vps4A

Julia D. Romano[1,*], Joshua Mayoral[2], Rebekah B. Guevara[2], Yolanda Rivera-Cuevas[3], Vern B. Carruthers[3], Louis M. Weiss[2,4] and Isabelle Coppens[1,*]

ABSTRACT

Intracellular pathogens exploit cellular resources through host cell manipulation. Within its nonfusogenic parasitophorous vacuole (PV), *Toxoplasma gondii* targets host nutrient-filled organelles and sequesters them into the PV through deep invaginations of the PV membrane (PVM) that ultimately detach from this membrane. Some of these invaginations are generated by an intravacuolar network (IVN) of parasite-derived tubules attached to the PVM. Here, we examined the usurpation of host ESCRT-III and Vps4A by the parasite to create PVM buds and vesicles. CHMP4B associated with the PVM/IVN, and dominant-negative (DN) CHMP4B formed many long PVM invaginations containing CHMP4B filaments. These invaginations were shorter in IVN-deficient parasites, suggesting cooperation between the IVN and ESCRT. In infected cells expressing Vps4A-DN, enlarged intra-PV structures containing host endolysosomes accumulated, reflecting defects in PVM scission. Parasite mutants lacking *T. gondii* (Tg)GRA14 or TgGRA64, which interact with ESCRT, reduced CHMP4B-DN-induced PVM invaginations and intra-PV host organelles, with greater defects in a double knockout, revealing the exploitation of ESCRT to scavenge host organelles by *Toxoplasma*.

KEY WORDS: ESCRT, Parasitophorous vacuole membrane, *Toxoplasma gondii* parasite, Mammalian organelle scavenging, Nutrient uptake

INTRODUCTION

Biotrophic microbes adapt to life inside host cells by evading host responses to infection and by exploiting the surrounding resources to promote multiplication. The apicomplexan protozoan *Toxoplasma gondii* is an obligate intracellular parasite that invades mammalian cells and creates its own replicative niche, the parasitophorous vacuole (PV), in the host cell cytoplasm. One critical factor for the success of *Toxoplasma* post invasion is the secretion of unique proteins from parasite-dense granule organelles that transform the PV into a replicative niche and modify the host cell. These proteins, usually named GRAs (64 so far), exert broad functions ranging from nutrient uptake, host organelle attraction and protein export from the PV into the host cell to control cellular signaling pathways, in particular those involved in innate immune responses and the cell cycle (reviewed in Mercier and Cesbron-Delauw, 2015; Panas and Boothroyd, 2021; Griffith et al., 2022).

Within *Toxoplasma*-infected cells, many cellular structures are reorganized and intercepted by the parasite. The host microtubular network is rearranged around the PV, allowing host organelles translocating along microtubules to cluster near the PV. Some microtubules create invaginations of the PV membrane (PVM) in which host organelles are engulfed (Coppens et al., 2006). Inside the PV, membranous tubules secreted by the parasite form an intravacuolar network (IVN) stabilized by two tubulogenic proteins, *T. gondii* (Tg)GRA2 and TgGRA6 (Sibley et al., 1995; Mercier et al., 2002; Bittame et al., 2015). Some IVN tubules connect to the PVM (de Souza and Attias, 2015; Magno et al., 2005) and form open conduits entrapping host organelles, resulting in their sequestration into the PV (Coppens et al., 2006; Romano et al., 2017; Hartman et al., 2022). *Toxoplasma* mutants with a defective IVN (Δ*gra2* and Δ*gra2*Δ*gra6*) have a reduced number of intra-PV host organelles. *Toxoplasma* secretes a phospholipase TgLCAT into the PV that localizes to IVN membranes surrounding internalized host organelles and destabilizes membranes by producing lysophospholipids from the release of fatty acids from phospholipids (Pszenny et al., 2016).

We have previously observed that host organelles, initially trapped in PVM invaginations, accumulate in the PV center, suggesting dissociation from the PVM (Romano et al., 2017). Tubule detachment from the PVM might be analogous to the biogenesis of intralumenal vesicles (ILVs) from budded portions of the limiting membrane of multivesicular bodies (MVBs), mediated by endosomal sorting complex required for transport (ESCRT) components, with the ESCRT-III complex and the associated AAA ATPase Vps4 (collectively referring to Vps4A and Vps4B) responsible for membrane scission (Piper and Katzmann, 2007; Schöneberg et al., 2017). The core ESCRT machinery can be subdivided into distinct subcomplexes (ESCRT-I, ESCRT-II and ESCRT-III) and accessory proteins, e.g. apoptosis-linked gene 2 (ALG-2, also known as PDCD6) and ALG-2-interacting protein X (ALIX, also known as PDCD6IP) (Vietri et al., 2020; Schöneberg et al., 2017). ESCRT-III directly reshapes and severs membranes in conjunction with Vps4, whereas the other subcomplexes and accessory proteins are involved in targeting and activating ESCRT-III (Vietri et al., 2020; Schöneberg et al., 2017; Pfitzner et al., 2021). ESCRT-III is composed of oligomers of charged multivesicular body proteins (CHMPs), e.g. CHMP2A, CHMP2B, CHMP3, CHMP4A and CHMP4B, with the CHMP4 proteins as the most abundant components (Teis et al., 2008; Schöneberg et al., 2017; Vietri et al., 2020). Through an auto-inhibition domain, CHMP proteins form inactive monomers in the cytosol, and upon release of

[1]Department of Molecular Microbiology and Immunology, Johns Hopkins University Bloomberg School of Public Health, Baltimore, MD 21205, USA. [2]Department of Pathology, Albert Einstein College of Medicine, Bronx, NY 10461, USA. [3]Department of Microbiology and Immunology, University of Michigan Medical School, Ann Arbor, MI 48109, USA. [4]Department of Medicine, Albert Einstein College of Medicine, Bronx, NY 10461, USA.

*Authors for correspondence (icoppens@jhsph.edu; jromano2@jhu.edu)

J.D.R., 0000-0001-8956-7377; J.M., 0000-0003-0859-2226; R.B.G., 0000-0002-8040-3453; Y.R.-C., 0000-0001-8389-5724; V.B.C., 0000-0001-6859-8895; L.M.W., 0000-0002-0357-7396; I.C., 0000-0001-5549-2362

Handling Editor: Michael Way
Received 26 April 2022; Accepted 19 January 2023

Journal of Cell Science (2023) 136, jcs260159. doi:10.1242/jcs.260159

auto-inhibition, activated CHMP proteins polymerize into filaments on membranes and adopt a variety of secondary shapes, resulting in membrane remodeling and scission (Alonso Y Adell et al., 2016; Cashikar et al., 2014; Harker-Kirschneck et al., 2019).

The association of host ESCRT components with the PV of *Toxoplasma* has recently become an active area of research. *Toxoplasma* recruits and utilizes host ALIX and tumor susceptibility gene 101 protein (TSG101) from ESCRT-I during parasite invasion (Guérin et al., 2017). A proximity-labeling study on *Toxoplasma*-infected fibroblasts to identify host proteins at the PV revealed that a PVM reporter biotinylated several host ESCRT components (e.g. ALIX, ALG-2, TSG101, VPS28, CHMP4B and CC2D1A) (Cygan et al., 2021). Two concomitant studies using co-immunoprecipitation and proximity-based biotinylation identified two *Toxoplasma* proteins on the PVM/IVN that interact with host ESCRT proteins: TgGRA14 (interacting with e.g. ALIX, ALG-2, TSG101 and CHMP4A/B) (Rivera-Cuevas et al., 2021) and TgGRA64 (interacting with e.g. TSG101, VPS37A, VPS28, CHMP4B and ALG-2) (Mayoral et al., 2022). Some of these host ESCRT components have been shown to associate with the PV: ALIX and ALG-2 localize as puncta on the PV (Cygan et al., 2021) and TgGRA14 influences PV recruitment of TSG101 (Rivera-Cuevas et al., 2021). The uptake of host cytosolic proteins by *Toxoplasma* (Dou et al., 2014) is reduced in mammalian cells ectopically expressing the Vps4A^{EQ} dominant-negative (DN) mutant (which has the glutamate at position 228 in the ATPase active site replaced by a glutamine) or by Δ*gra14* mutant parasites (Rivera-Cuevas et al., 2021).

We hypothesize that host ESCRT machinery diverted by *Toxoplasma* is involved in the scission of IVN tubules containing host vesicles from the PVM. In this study, using fluorescence microscopy and transmission electron microscopy (TEM), we analyzed the recruitment of the ESCRT-III component CHMP4B and Vps4A to the PV to assess their impact on PVM remodeling for host organelle internalization. We also examined the distribution of several host ESCRT components on the IVN where intra-PV host organelles accumulate. Finally, we compared the ability of wild-type (WT) and mutant parasites lacking *gra14* and/or *gra64* to scavenge host Rab11 vesicles.

RESULTS

The endogenous ESCRT-III component CHMP4B is recruited to the *Toxoplasma* PV

A principal target of intravacuolar *Toxoplasma* is the endosomal recycling pathway in the host mammalian cell (Romano et al., 2017; Hartman et al., 2022). Rab11A localizes to the endocytic recycling compartment (ERC), recycling endosomes and the trans-Golgi network to regulate vesicular trafficking between these compartments (Maxfield and McGraw, 2004). Endogenous Rab11A in uninfected cells localized as puncta throughout the cytoplasm with a concentration near the nucleus where the ERC is predominantly located (Fig. 1A). In *Toxoplasma*-infected cells, the PV localizes near the host ERC and Rab11A-positive vesicles. *Toxoplasma* internalizes host GFP–Rab11A vesicles into the PV (seen for 89% of all PVs examined) using IVN tubules appended to the PVM, creating conduits into the PV (Coppens et al., 2006; Romano et al., 2017). We detected several endogenous Rab11A foci on IVN patches (indicated by TgGRA7 staining) (Fig. 1A), as previously reported (Romano et al., 2017). The exploitation of IVN tubules to sequester host organelles was further confirmed by TEM of infected cells incubated with low density lipoprotein (LDL)–gold particles to track host endolysosomes. Data illustrate IVN tubules attached to the PVM (Fig. 1Ba), with some containing LDL-containing organelles in the process of penetrating a tubule lumen (Fig. 1Bb) or inside a tubule distant from the PVM (Fig. 1Bc), suggesting scission from the PVM. To examine whether host ESCRT machinery is recruited by *Toxoplasma* to induce PVM buds and long invaginations into the PV lumen to facilitate host organelle internalization via the IVN, we monitored the distribution of CHMP4B upon *Toxoplasma* infection. HeLa cells stably expressing GFP–CHMP4B (Jouvenet et al., 2011) were infected for 6 or 24 h to compare with uninfected cells. GFP–CHMP4B was detected in the nucleus and the cytoplasm, in addition to some defined vesicles in uninfected HeLa cells (Fig. 1Ca); this specific localization was confirmed by silencing of GFP–CHMP4B (Fig. S1A). In cells infected for 6 h, the staining for GFP–CHMP4B was observed around the PV (Fig. 1Cb) and often as well-defined puncta along the edge of the PVM (identified with antibodies against TgGRA7) (Fig. 1Cc). At 24 h post-infection (p.i.), the GFP–CHMP4B signal was more prominent on several areas of the PVM and patches of the IVN (Fig. 1Cd,e), suggesting CHMP4B recruitment. Measurements of Mander's colocalization coefficients (MCCs) suggested a correlation between the GFP–CHMP4B and TgGRA7 (PVM/IVN) signals. To examine the role of the IVN in CHMP4B internalization into the PV, we monitored GFP–CHMP4B in HeLa cells infected with the Δ*gra2*Δ*gra6* mutant that has a defective IVN (Mercier et al., 2002) and is deficient in host vesicle internalization (Romano et al., 2017). GFP–CHMP4B puncta were observed along the Δ*gra2*Δ*gra6* PV periphery, with few puncta detected in the PV lumen (Fig. 1Cf).We assessed the intra-PV distribution of host GFP–CHMP4B relative to PV-associated Rab11A vesicles and observed an accumulation of GFP–CHMP4B and Rab11A puncta along the edge of the PV (Fig. S1Ba) with a partial overlap of a few puncta (Fig. S1Bb), suggesting a possible involvement of CHMP4B in host vesicle internalization into the PV in synergy with IVN tubules.

Dominant-negative CHMP4B tagged with mEmerald at the N- or C-terminus is targeted to different locations at the PV

Host CHMP4B partially localizes to the PVM and the IVN, supporting the hypothesis that *T. gondii* utilizes the host ESCRT-III complex during infection. CHMP4B undergoes a conformation change that exposes C-terminal domains to recruit Vps4 and other effectors, such as ALIX, enabling membrane binding, oligomerization and scission (Tang et al., 2015; Muziol et al., 2006; Lata et al., 2008; Obita et al., 2007; McCullough et al., 2008; Henne et al., 2012; Lin et al., 2005). Ectopic expression of CHMP proteins with bulky protein tags on either the N- or C-terminus could interfere with conformational changes and cause DN effects, leading to the formation of enlarged endosomal 'class E-like' compartments (Martin-Serrano et al., 2003; Howard et al., 2001; von Schwedler et al., 2003). Taking advantage of the DN effect that ESCRT-III subunits tagged with large fluorophores have on complex activity, we investigated the DN effect of CHMP4B on the PV. We overexpressed CHMP4B tagged with mEmerald (mEm) either at the N-terminus (mEm–CHMP4B) or the C-terminus (CHMP4B–mEm) in HeLa cells. In uninfected cells expressing either construct, large punctate structures consistent with enlarged class E compartments containing tagged CHMP4B were observed throughout the cytoplasm (Fig. 2A,B). In cells expressing mEm–CHMP4B and infected with WT parasites for 20 h, mammalian class E compartments surrounded the PV and discrete mEm–CHMP4B puncta were detected on the PVM and inside the PV within IVN patches (Fig. 2A; Fig. S2A). In cells infected with the IVN mutant Δ*gra2*Δ*gra6*, mEm–CHMP4B compartments

Journal of Cell Science (2023) 136, jcs260159. doi:10.1242/jcs.260159

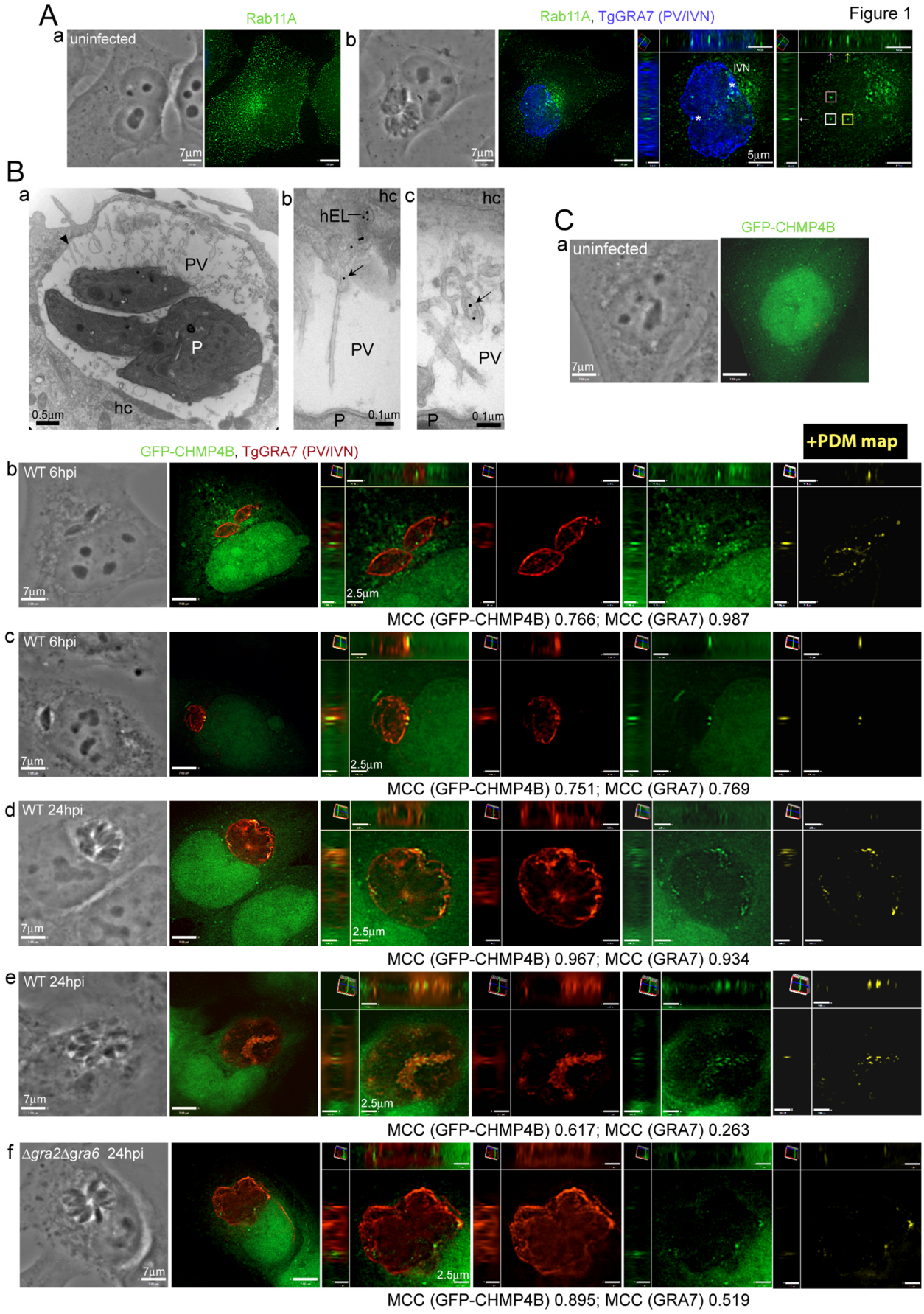

Fig. 1. See next page for legend.

Journal of Cell Science (2023) 136, jcs260159. doi:10.1242/jcs.260159

Fig. 1. Localization of CHMP4B and Rab11A in infected cells. (A) Immunofluorescence assay (IFA). Uninfected and infected (20 h) HeLa cells were fixed and immunostained for Rab11A (green, a,b) and TgGRA7 (blue, b). Individual *z*-slices and cropped images of the PV (orthogonal views) are shown. Intra-PV Rab11A puncta are indicated in squares and marked by arrows. Asterisks show patches of the IVN. (B) Transmission electron microscopy (TEM). Infected VERO cells were incubated with LDL–gold particles for 24 h before fixation. The arrowhead (a) shows an IVN tubule attached to the PVM. The arrows (b,c) indicate LDL-containing organelles penetrating (b) or within (c) a tubule lumen. hc, host cell; hEL, host endolysosome; P, parasite. (C) IFA. HeLa cells stably expressing GFP–CHMP4B that were uninfected (a) or infected for 6 (b,c) or 24 h (d–f) with WT (b–e) or Δ*gra2*Δ*gra6* (f) parasites were immunostained for TgGRA7. A positive product of the difference from the mean (PDM) image is shown, highlighting in yellow the voxels where the intensity values of GFP–CHMP4B and TgGRA7 are above their respective means (overlapping signal). Both PDM images and MCCs were thresholded for background, as described in Materials and Methods. Individual *z*-slices and cropped images of the PV (orthogonal views) are shown. Images are representative of three independent experiments. hpi, hours post infection.

associated with the PV were observed but no puncta were observed within, and faint mEm–CHMP4B staining was observed along the PVM (Fig. 2A). In contrast, in infected cells expressing CHMP4B–mEm, the signal was predominantly distributed on the PVM of both WT and Δ*gra2*Δ*gra6* parasites, and no puncta were observed within the PV (Fig. 2B; Fig. S2B).

Next, we monitored CHMP4B–mEm recruitment at the PV over time by measuring the colocalization of CHMP4B–mEm and TgGRA7 at the PVM using MCC. We observed that CHMP4B–mEm progressively associated with the PVM (Fig. S2C), with a mean MCC value for TgGRA7 of 0.232 at 20 min p.i., increasing to 0.716 at 8 h p.i. (a time point typically corresponding to the first round of *Toxoplasma* division) (Fig. 2C; Fig. S2C). The mean MCC values for CHMP4B–mEm also trended higher as the infection progressed (Fig. S2C,D). At a later point after infection (40 h p.i.) prior to *Toxoplasma* egress, CHMP4B–mEm staining was mainly detected on the PVM, suggesting continuous recruitment by the parasite (Fig. 2D). Interestingly, CHMP4B association with the PV occurred even when the bulk of CHMP4B–mEm localized far from the PV, e.g. on the other side of the host nucleus (Fig. 2E), and was also observed along projections of the PVM that extend into the host cytosol (Fig. S2C, 8 h p.i.).

To scrutinize the association of mEm-tagged CHMP4B with the PVM in finer detail, we performed immuno-electron microscopy (immuno-EM) using anti-GFP antibodies on infected cells expressing either construct. Within the mammalian cell, gold particles localized mEm–CHMP4B and CHMP4B–mEm to multilamellar class E compartments (Fig. 2F). In infected cells, PV-associated mEm–CHMP4B predominantly distributed to IVN tubules, whereas gold particles detecting CHMP4B–mEm were observed aligned along the PVM, covering the PV entirely on each cryosection. Taken together, these observations highlight that after induction of DN CHMP4B in infected cells, *Toxoplasma* actively recruits CHMP4B to the PV, but the final destination of this protein on the PV differs according to position of the mEmerald tag. mEm–CHMP4B is internalized into the PV, whereas CHMP4B–mEm is trapped in this membrane, suggesting that the C-terminal mEmerald tag allows PVM recruitment of CHMP4B but interferes with later scission steps from this membrane.

The PVM containing host CHMP4B–mEm invaginates and buds into the PV lumen

We examined in greater detail and resolution the ultrastructure of the massive recruitment of CHMP4B–mEm at the PVM in ultra-thin resin-embedded cells. In non-transfected cells, the PVM had a relatively flat appearance with closely apposed host mitochondria and endoplasmic reticulum elements (Fig. 3Aa). These host organelles form intimate association with the PVM mediated by parasite proteins (de Melo et al., 1992; Melo and De Souza, 1997; Sinai et al., 1997; Pernas and Boothroyd, 2010; Pernas et al., 2014) but are never detected within the PV, unlike host endocytic organelles. Higher-magnification observations revealed PVM indentations containing host LDL-containing organelles, seemingly targeted by tubules of the IVN as a point of anchorage and fusion for host organelle internalization into the PV (Fig. 3Ab). Infected cells transfected with CHMP4B–mEm were identified by the presence of class E compartments in the host cytosol. Unlike PVs in non-transfected cells, the PVM containing CHMP4B–mEm displayed a corrugated morphology, with tubular (up to 450 nm-long) and numerous invaginations (often spaced less than ∼50 nm from each other) detected over the entire surface of this membrane (Fig. 3B). In transfected cells expressing CHMP4B–mEm and infected with Δ*gra2*Δ*gra6* parasites, the PVM also contained CHMP4B–mEm, although to a lesser extent than WT PVM (Fig. 1C), and underwent the same deformation process with the generation of nanosized buds away from the host cytoplasm (Fig. 3C). However, the PVM buds in the Δ*gra2*Δ*gra6* mutant were rarer, further apart and smaller in size (∼80 nm long), suggesting that IVN tubules contribute to supply membranes at PVM bud sites in WT PVs.

Replicating *Toxoplasma* usually distribute radially, forming a rosette-like structure inside the PV. However, upon CHMP4B–mEm recruitment, the parasites were often spatially disorganized within the PV, with very little recruitment of host mitochondria and the endoplasmic reticulum at the PVM (Fig. S3A). Furthermore, some PVs dually stained for CHMP4B and TgGRA7 appeared ‘empty’, a sign of *Toxoplasma* deterioration (Fig. S3B,C). In cells expressing CHMP4B–mEm, the enumeration of parasites per PV at 20 h p.i. showed that ∼35% of PV contained eight parasites, similarly to cells expressing mEm–CHMP4B, but uniquely ∼15% of PV did not harbor any parasites (Fig. S3D).

High-magnification observations of the PVM containing host CHMP4B–mEm on longitudinal sections of tubular invaginations revealed regular constrictions in the horizontal plane that continued along the length of the tubular structures, resulting in a reduction of the membrane tube radius (Fig. 3D). The overall diameter of the PVM tubules was uniform (105±10 nm, indicated as mean±s.d.). Our morphological analyses suggest sequential steps in the formation of PVM tubular invaginations. Initially, distinct filamentous structures, likely CHMP4B polymers, accumulated at many areas of the PVM. Then, these confined areas that were decorated with filaments evolved from flat to small buds (Fig. 3Ea). Filaments were detected in the interior of the buds, organized into rings attached to membrane (Fig. 3Eb). Finally, concomitant with the incorporation of filaments into PVM buds, these buds transformed progressively into tubules up to 8 µm long that underwent constriction with decreased diameter (Fig. 3Ec). Immunostaining for CHMP4B confirmed the presence of gold particles coating the interior of PVM invaginations (Fig. 3Fa). Stabilized ESCRT-III filaments including CHMP4B polymers, are frequently organized into spirals on curved membranes (Cashikar et al., 2014). A similar organization of CHMP4B filaments was observed within PVM tubules, as observed in a tangential section showing gold particle distribution in a spiraled pattern (S shape) (Fig. 3Fb) and on transverse sections of PVM tubules showing CHMP4B filaments (characterized by a high electron density layer beneath the tubule

Journal of Cell Science (2023) 136, jcs260159. doi:10.1242/jcs.260159

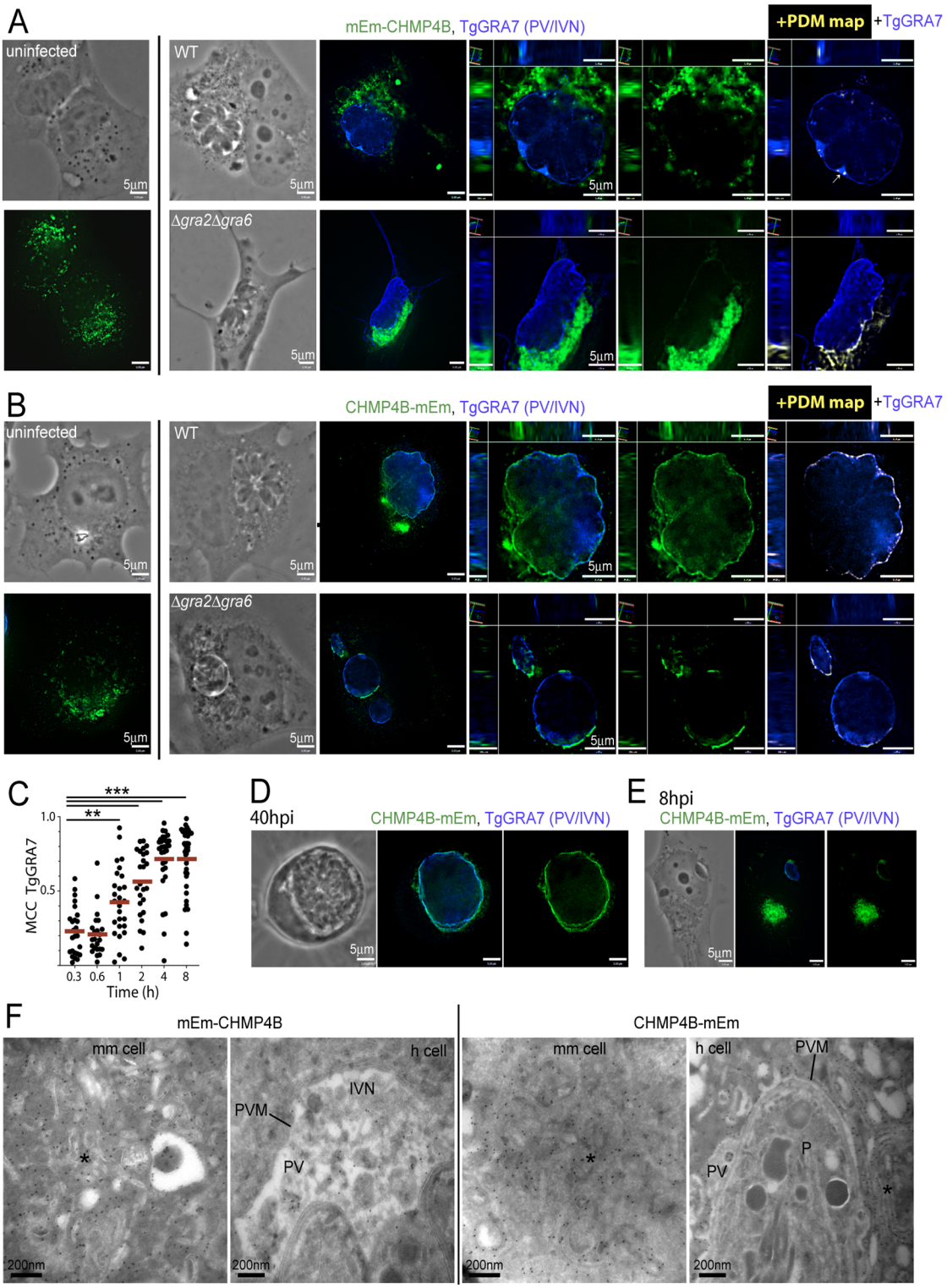

Fig. 2. Differential PV localization of CHMP4B tagged with mEmerald on its N- or C-terminal. (A,B) IFA. HeLa cells were transiently transfected with mEm–CHMP4B (A) or CHMP4B–mEm (B). Uninfected cells (left) and cells infected with WT or *Δgra2Δgra6* parasites for 20 h (right) were fixed and immunostained for TgGRA7. The arrow in A shows CHMP4B staining on the IVN. Individual *z*-slices and cropped images of the PV (orthogonal views) are shown, along with positive PDM images overlaid with TgGRA7 signal. (C) IFA. HeLa cells transiently transfected with CHMP4B–mEm were infected with WT parasites at the indicated times, fixed and immunostained for TgGRA7. Mander's correlation coefficients (MCC, TgGRA7) were calculated with Volocity. Dot blots are shown with red bars indicating the mean. Number of PVs measured: 0.3 h, 25; 0.6 h, 23; 1 h, 27; 2 h, 25; 4 h, 30; 8 h, 40; from one representative experiment. $^{**}P$=0.0098; $^{***}P$<0.0001; one-way ANOVA with Tukey's multiple comparisons. (D,E) IFA. HeLa cells transiently transfected with CHMP4B–mEm were infected with WT parasites for 40 (D) or 8 h (E), fixed and immunostained for TgGRA7. Individual *z*-slices are shown. (F) Immuno-EM. HeLa cells transiently transfected with either mEm–CHMP4B (left panels) or CHMP4B–mEm (right panels) and either uninfected [mammalian (mm) cells] or infected [host (h) cells] with WT parasites ('P') for 20 h. Asterisks show class E-like compartments. Images are representative of two independent experiments.

Journal of Cell Science (2023) 136, jcs260159. doi:10.1242/jcs.260159

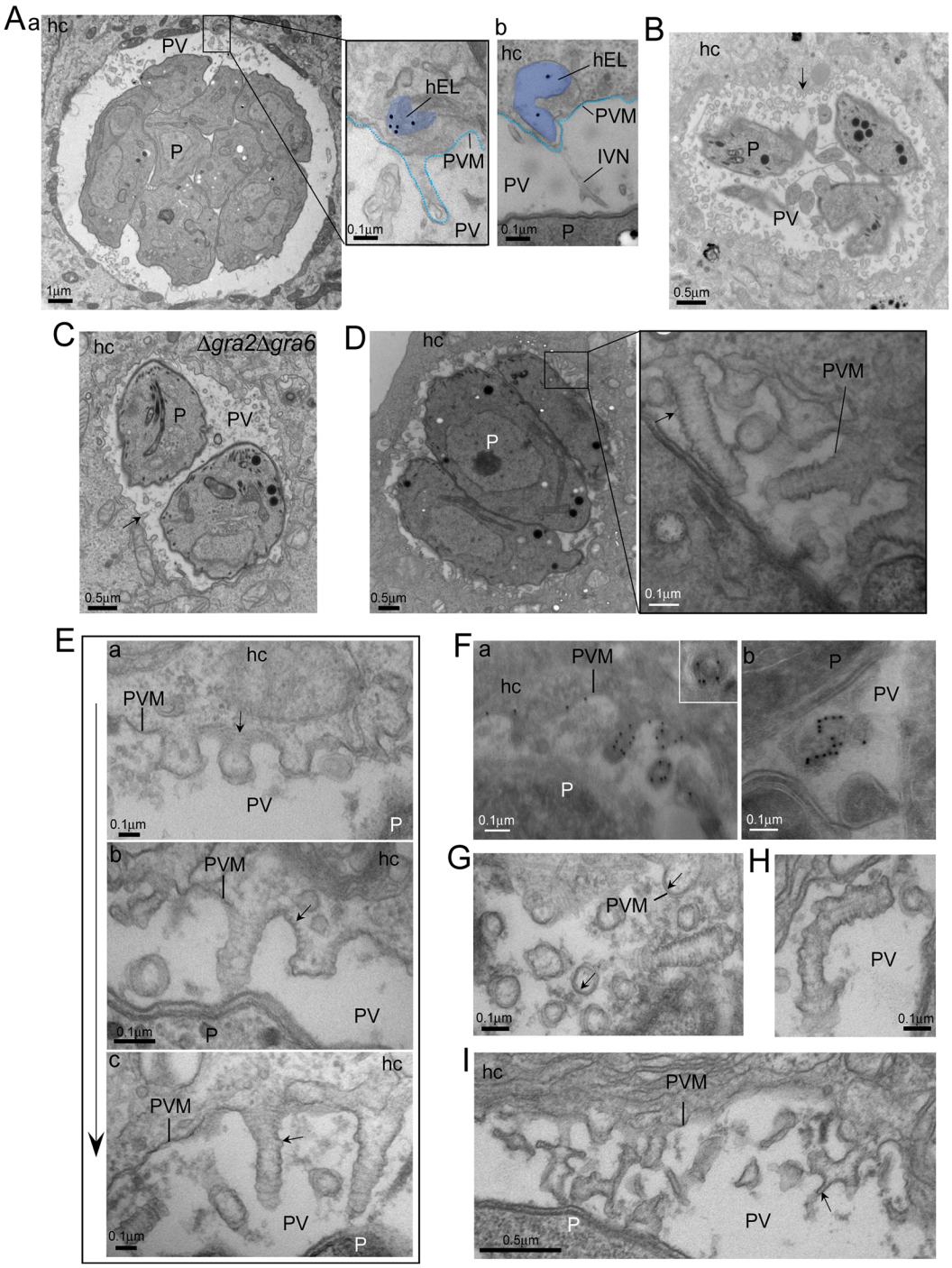

Fig. 3. Ultrastructure of PV in HeLa cells expressing CHMP4B–mEm. (A–I) TEM. (A) Infected HeLa cells were incubated with LDL–gold particles for 20 h to track host endolysosomes (hEL, pseudocolored in blue; inset, panels a,b). The blue dotted lines indicate the PVM. (B,C) HeLa cells transfected with CHMP4B–mEm and infected with WT parasites (B) showing extensive PVM remodeling, or infected with *Δgra2Δgra6* parasites (C) showing fewer and smaller tubules at the PVM. Arrows show PVM buds or tubules. (D–I) Infected CHMP4B–mEm-expressing HeLa cells showing numerous large tubular structures with regular constrictions (arrow in D). In E, panels a–c show examples of different PVM tubule lengths (arrows). In F, immunogold staining with the anti-GFP antibody shows gold particles within tubules; the inset in panel a shows a transversal section of a tubule with gold particles on an inner structure corresponding to CHMP4B filaments. In G, transverse sections of tubules showing CHMP4B filaments inside tubules (arrows) identifiable by their higher electron density compared to that of the tubular membrane. Panels H,I show representative images of curled or ramified tubules. The arrow in I shows a smaller tubule, likely from the IVN, attached to a large, constricted tubule. Images are representative of three independent experiments. hc, host cell; P, parasite.

membrane) forming a partial ring that might reflect a spiral configuration (Fig. 3G). We noticed that some PVM tubules appeared slightly bent (Fig. 3D,H) and branched, with some bifurcations reminiscent of IVN tubules that might have fused with large PVM tubules containing CHMP4B filaments (Fig. 3D,I).

Taken together, these observations suggest that host CHMP4B recruited at the PVM assembles into filaments at the membrane

Journal of Cell Science (2023) 136, jcs260159. doi:10.1242/jcs.260159

surface, driving tubular invaginations away from the cytoplasm. Within PVM tubules, assembled CHMP4B filaments narrow the tubule, similar to the CHMP4A internal coat on negatively curved membranes, to draw membranes together to the fission point (McCullough et al., 2015).

FLAG-tagged CHMP4B localizes to the PVM and as enlarged puncta within the PV close to Rab11A vesicles

Overexpression of CHMP proteins fused to a protein tag leads to DN effects, presumably due to the bulky tag interfering with the inhibitory intramolecular interactions necessary to keep CHMP proteins in an inactive soluble form. Thus, we opted to use CHMP4B tagged with a FLAG tag (eight amino acids, ~1 kDa) at the N-terminus (FLAG–CHMP4B). Previous studies reported FLAG–CHMP4B localization as a punctate pattern upon transient transfection in HeLa cells and a more diffuse cytoplasmic distribution upon stable expression in HEK293 cells, with vesicle-like structures observed in 5% of the cells (Katoh et al., 2003). We confirmed the localization of FLAG–CHMP4B as disperse puncta, partially concentrated in the perinuclear region in HeLa cells, as a result of overexpression (Fig. 4Aa). In HeLa cells infected with *T. gondii* for 20 h, three patterns for FLAG–CHMP4B distribution were observed: 66% of cells displayed a FLAG–CHMP4B signal throughout the host cell with partial localization to the PV, whereas 34% exhibited a signal predominantly associated with the PV (Fig. 4Ab), and within this population, FLAG–CHMP4B was observed either as very large intra-PV puncta (up to 1 µm in diameter) near IVN patches (23%) or all along the PVM (11%). The majority of large intra-PV puncta containing FLAG–CHMP4B had a torus shape that colocalized with TgGRA7, suggesting that CHMP4B puncta are derived from the PVM (Fig. 4Ac).

We assayed whether CHMP4B puncta localized in close proximity to intra-PV Rab11A puncta by infecting HeLa cells expressing FLAG–CHMP4B and immunostaining for Rab11A. Several intra-PV FLAG–CHMP4B and Rab11A puncta were detected in patches of TgGRA7 signals, presumably overlapping with the IVN and, to a lesser extent, with each other (Fig. 4B; Fig. S4A,B). We next conducted TEM observations to scrutinize the PVM in infected HeLa cells expressing FLAG–CHMP4B. In the cytoplasm of transfected cells, many vesicles of variable size were generated (Fig. S4C). In all PVs examined in transfected cells, no PVM tubulation or unusual remodeling was observed (Fig. S4D), similar to the PVs in cells expressing mEm–CHMP4B (Fig. 2F). However, the PV lumen contained several large unique structures (up to 700 nm in diameter) composed of numerous vesicles (20–100 nm in diameter) encircled by membrane and close to the IVN, with some attached to the PVM (Fig. 4C). These large multivesicular structures were reminiscent of large CHMP4B puncta surrounded by TgGRA7, detected by immunofluorescence assay (IFA) (Fig. 4Ab). Based on size and electron density, we interpreted the nature of the luminal vesicles to likely be host endosomal vesicles formed upon CHMP4B overexpression that are subsequently internalized into the PV and surrounded by the PVM.

To assess whether IVN tubules could be involved in the internalization of FLAG–CHMP4B into the PV, FLAG–CHMP4B-expressing cells were infected with Δ*gra2*Δ*gra6* parasites. Two patterns for FLAG–CHMP4B distribution in infected cells were discernible: partial staining of the PV with the bulk in the host cytoplasm (58%) or preponderant PV labeling (42%) with no intra-PV puncta detected (Fig. 4D), suggesting that IVN tubules are important for the accumulation of FLAG–CHMP4B in the PV.

Dominant-negative Vps4A results in PV swelling and accumulation of enlarged intra-PV membrane-bound structures containing host organelles

Vps4A and Vps4B proteins are members of a class of hexameric AAA^+ ATPases that disassemble protein complexes without degradation. Vps4 enzymes contain an N-terminal microtubule interacting and trafficking (MIT) domain that binds to the tails of ESCRT-III proteins. ESCRT-III–Vps4 complexes assemble within the necks of membrane tubules and convert the energy of ATP hydrolysis into pulling forces that sever the tubules (Yang et al., 2015). Vps4 is also required for the recycling of ESCRT-III from membrane-bound filaments back to the cytosol (Babst et al., 1998; Bishop and Woodman, 2000; Lin et al., 2005). As Vps4 is involved in many cellular processes that require membrane remodeling and scission, we hypothesize that *Toxoplasma* exploits host Vps4 along with CHMP4B to facilitate PVM budding and scission of IVN tubules, containing host organelles, from the PVM. We analyzed the distribution of Vps4A in infected cells transfected with mCherry–Vps4A. In transfected HeLa cells, we observed a perivacuolar staining for mCherry–Vps4A with puncta associated with the PV (Fig. 5A). Expression of the DN mutant $Vps4A^{EQ}$ (with a mutation in the ATPase active site) causes a class E phenotype with an aggregation of MVBs due to blockade of ESCRT-dependent ILV formation (Bishop and Woodman, 2000). We examined whether $Vps4A^{EQ}$-mediated ESCRT-III dysfunction impacted PV sequestration of host organelles. In HeLa cells transfected with mCherry–$Vps4A^{EQ}$, enlarged endosomal vacuoles were observed, with some surrounding the PV (Fig. 5A), as observed previously (Rivera-Cuevas et al., 2021). We noticed that in cells expressing mCherry–$Vps4A^{EQ}$, the PVM appeared less well defined, as seen by an abnormal TgGRA7 staining almost filling the PV lumen, opposed to a more circumferential TgGRA7 staining on the PVM in cells expressing mCherry–$Vps4A^{WT}$. Using anti-Rab11A antibodies, some host Rab11A vesicles could be identified that appeared to associate with the PV; however, due to the abnormal morphology of the PVM, we were unable to determine whether their localization was outside or inside the PV.

To investigate the morphological PVM defects and assess the PV for host organelle sequestration, we conducted TEM analyses on infected HeLa cells transfected with mCherry–$Vps4A^{EQ}$. Expectedly, in transfected cells incubated with LDL–gold particles, we detected gold particles in enlarged multilamellar organelles that accumulated in the host cytoplasm (Fig. 5B), with some clustering around the PV (Fig. 5C). A striking observation was the presence of large PVM-derived membranous whorls that expanded into the vacuolar space (Fig. 5C,D); some IVN tubules were seen attached to these enlarged structures (Fig. 5D, right inset). Intra-PV LDL–gold-containing organelles amassed in bundles forming large multi-vesiculated entities up to 900 nm in diameter (Fig. 5E), compared to the small intra-PV, LDL–gold-containing organelles in the PVs of non-transfected cells (~200 nm in diameter) (Fig. 1Bc) (Coppens et al., 2006). These LDL–gold-containing organelles remained close to the PVM (average distance of ~0.25 µm), whereas in WT PVs, many were present in the PV center (Fig. 5F). Taken together, these observations reveal that DN Vps4A causes abnormal PVM proliferation with host organelles entrapped in PVM folds, suggesting retardation of scission activities owing to impaired Vps4A functions.

Journal of Cell Science (2023) 136, jcs260159. doi:10.1242/jcs.260159

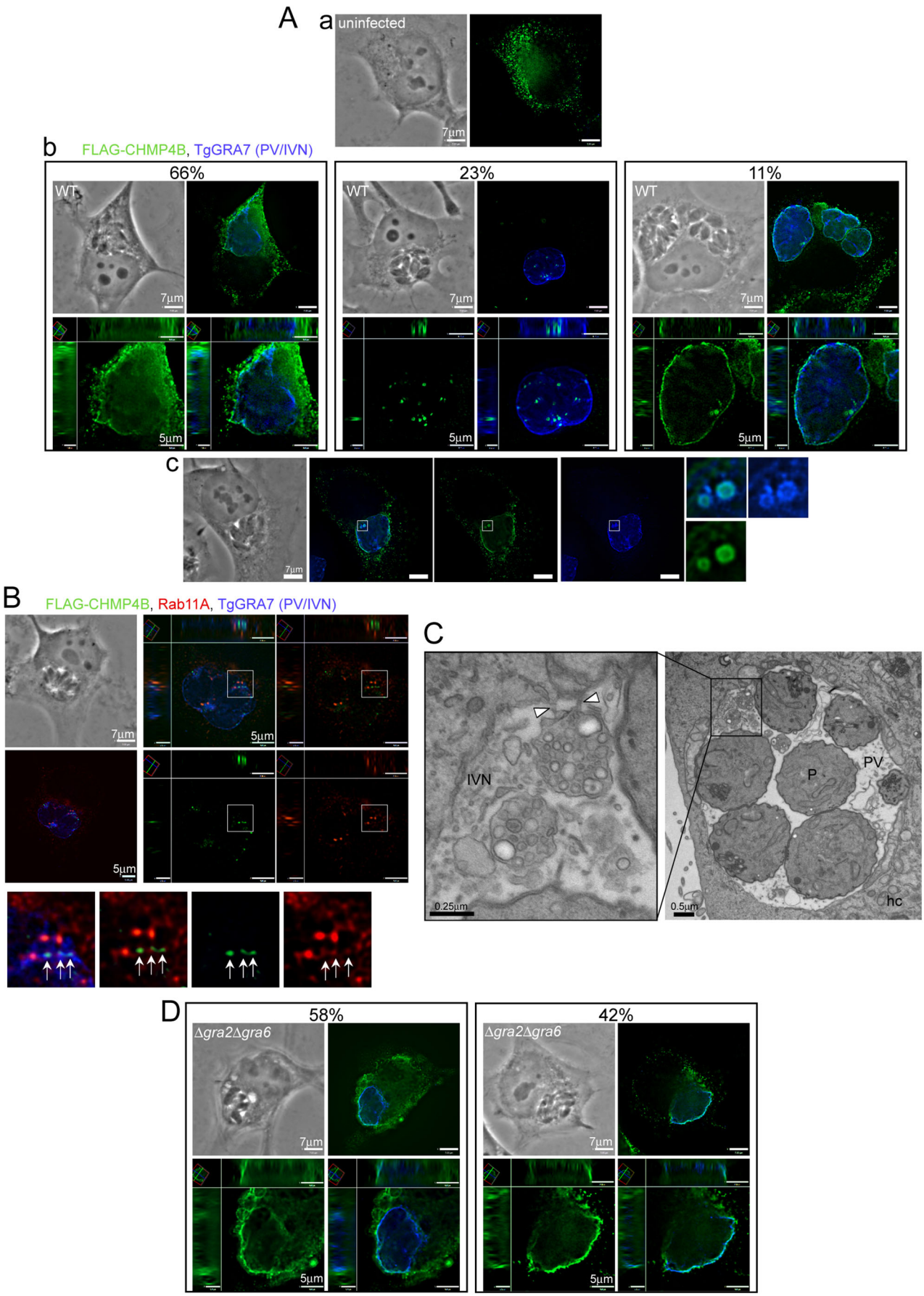

Fig. 4. See next page for legend.

Journal of Cell Science (2023) 136, jcs260159. doi:10.1242/jcs.260159

Fig. 4. Association of FLAG–CHMP4B with the PV. (A) IFA. HeLa cells were transiently transfected with FLAG–CHMP4B and either not infected (a) or infected (b,c) for 20 h, fixed and immunostained for FLAG and TgGRA7. The percentages of infected cells with the displayed morphology are shown. Enlarged regions (marked by squares) show overlap between CHMP4B and TgGRA7 in a torus-like vesicle. (B) IFA. HeLa transiently transfected with FLAG–CHMP4B were infected for 20 h, fixed and immunostained for FLAG, Rab11A and TgGRA7. Enlarged regions (marked by squares) show overlap between intra-PV CHMP4B and Rab11A (arrows) on the IVN marked by TgGRA7. Individual *z*-slices and cropped images of the PV (orthogonal views) are shown (A,B). (C) TEM. Infected HeLa expressing FLAG–CHMP4B showing accumulation of large intra-PV multi-vesicular structures, some with a visible connection with the PVM. The white arrowheads show points of connection with the PVM. hc, host cell; P, parasite. (D) HeLa cells expressing FLAG–CHMP4B infected with Δ*gra2*Δ*gra6* parasites as in A. The percentages of infected cells with the displayed morphology are shown. Images are representative of two independent experiments.

Intra-PV Rab11A is surrounded by host ALG-2, an interacting partner of the ESCRT accessory protein ALIX

The adaptor protein ALIX, the Bro1 domain of which binds to a C-terminal motif of CHMP4, participates in a variety of ESCRT-III-mediated membrane remodeling processes (McCullough et al., 2008). The Ca^{2+}-binding protein ALG-2 forms intramolecular interactions with ALIX in a Ca^{2+}-dependent manner (Sun et al., 2015). Host ALIX and ALG-2 have been shown to associate with the *Toxoplasma* PV as puncta along and within the PV (Cygan et al., 2021; Rivera-Cuevas et al., 2021). To investigate whether host ALIX or ALG-2 participates in host vesicle internalization into the PV, we examined the distribution of intra-PV ALIX or ALG-2 puncta relative to Rab11A vesicles. In infected GFP–Rab11A-expressing VERO cells transfected with HA-tagged ALIX, only a few intra-PV ALIX–HA puncta displayed a partial overlap with GFP–Rab11A (Fig. 6A). In comparison, the association of ALG-2–HA with the PVM and IVN was more prominent and numerous ALG-2–HA puncta partially overlapped with GFP–Rab11A (Fig. 6B). To assess the overlap of GFP–Rab11A and ALG-2–HA in finer detail, we performed dual immunogold labeling on ALG-2–HA-expressing cells. In the mammalian cytoplasm, gold particles were observed on membranes and vesicles associated with either Rab11A or ALG-2–HA, but none with both (Fig. 6Ca). Within the PV, however, both Rab11A and ALG-2–HA were detected on the same vesicular structures with Rab11A (10 nm gold particles) on the inside and ALG-2–HA (5 nm gold particles) were externally displayed (Fig. 6Cb–d). This illustrates that intra-PV Rab11A vesicles are surrounded by a membrane that contains ALG-2 (presumably derived from the PVM/IVN), suggesting a potential role for ALG-2 and, to a lesser extent, for ALIX in cooperating with CHMP4B at sites of PVM remodeling for host organelle sequestration.

The ESCRT-interacting proteins TgGRA14 and TgGRA64, secreted to the PVM, function synergistically in intra-PV Rab11A internalization

T. gondii secretes two dense granule proteins, TgGRA14 and TgGRA64, that physically interact with several ESCRT components and localize to the PVM and IVN post secretion (Rivera-Cuevas et al., 2021; Mayoral et al., 2022). We examined the contribution of TgGRA14 and TgGRA64 in ESCRT-mediated PVM functions. First, we compared the PV distribution of GFP–CHMP4B (low level of expression) among a strain lacking both *gra14* and *gra64* (Δ*gra14*Δ*gra64*), WT and Δ*gra2*Δ*gra6* parasites. GFP–CHMP4B was detected along the PVM of each strain, but few intra-PV GFP–CHMP4B puncta were observed, as were seen for Δ*gra2*Δ*gra6* PVs (Fig. 7A). This suggests that CHMP4B might associate with the PV independently of TgGRA14 and/or TgGRA64 but that these proteins are most likely involved in CHMP4B-mediated PVM invaginations. Inspection of Δ*gra14*Δ*gra64* ultrastructure did not reveal obvious defects of the PVM or host organelle association (Fig. 7Ba). The PV contained an IVN (Fig. 7Bb; Fig. S5Aa) and also abnormal fibrous structures appended to IVN tubules (Fig. S5Ab,c). No organellar abnormalities were observed for Δ*gra14* or Δ*gra14*Δ*gra64* parasites, except for the accumulation of starch-like amylopectin granules (Fig. 7Bc,d), a marker of stress (Coppin et al., 2003). Accumulation of amylopectin granules suggests that parasites lacking TgGRA14 and/or TgGRA64 probably undergo remodeling of their metabolism to cope with stress conditions, such as nutrient limitations.

Second, we investigated whether Δ*gra14*Δ*gra64* and Δ*gra14* parasites remodeled their PVM to create buds or invaginations in cells transfected with DN CHMP4B–mEm. Although the PVM of WT parasites displayed numerous, long tubular extensions enclosing CHMP4B–mEm filaments on each parasite section viewed (Fig. 7Ca), the PVM of both mutants exhibited sparse buds (Fig. 7Cb–d). In rare sections of either mutant, longer tubular invaginations were observed, containing inner filaments along the tubule membrane and displaying irregular constrictions (Fig. 7Da–c) or sometimes short ramifications (Fig. S5B). In 22% of Δ*gra14*Δ*gra64* sections, no PVM budding or bending induced by CHMP4B filaments was apparent, reflecting the rarity of PVM remodeling events in the double mutant (Fig. S5C).

Third, we compared the ability of Δ*gra14*, Δ*gra64*, Δ*gra14*Δ*gra64* and Δ*gra2*Δ*gra6* parasites to scavenge host Rab11A vesicles relative to that of WT parasites. The Δ*gra2*Δ*gra6* mutant was used as a control as it was previously shown to have a defect in host vesicle internalization (Romano et al., 2017). VERO cells expressing GFP–Rab11A were infected to assess the number, distance from the PV centroid and size of intra-PV GFP–Rab11A puncta. Compared to WT parasites, both Δ*gra14* and Δ*gra64* parasites showed a statistically significant decrease (25%) in the number of intra-PV host GFP–Rab11A puncta (Fig. 7E; Fig. S6A). A more pronounced reduction in puncta number was observed for Δ*gra14*Δ*gra64*, corresponding to a ∼45% decrease compared to WT parasites, although it was not as dramatic as for Δ*gra2*Δ*gra6* parasites (∼70% decrease). No differences were observed in the distance to the PV centroid or in the volume of intra-PV GFP–Rab11A puncta, except for Δ*gra2*Δ*gra6* (Fig. S6B,C).

TgGRA14 has been shown to co-immunoprecipitate with CHMP4B along with other ESCRT components (Rivera-Cuevas et al., 2021). Finally, we assessed the distribution of TgGRA14 relative to CHMP4B at the PV by infecting HeLa cells stably expressing CHMP4B for 6 and 24 h (Fig. 8A). Unlike TgGRA7 that localizes all around the PVM, TgGRA14 appeared to be more concentrated at some areas of the PV. Interestingly, the signal for GFP–CHMP4B was observed at the sites of TgGRA14 accumulation in distinct puncta. At 24 h p.i., TgGRA14 and GFP–CHMP4B were also observed in the same regions inside the PV. Such a co-distribution of TgGRA14 and GFP–CHMP4B at the PV is in accordance with the TgGRA14-CHMP4B interactions.

Collectively, our data indicate a connection between the poor ability of *Toxoplasma* lacking *gra14* and *gra64* to remodel the PVM and its reduced competency in sequestering intra-PV host vesicles. However, the retention of some activity reveals that other protein(s) might be able to recruit host ESCRT at the PVM and function analogously for host vesicle uptake. Our results suggest a synergistic

Journal of Cell Science (2023) 136, jcs260159. doi:10.1242/jcs.260159

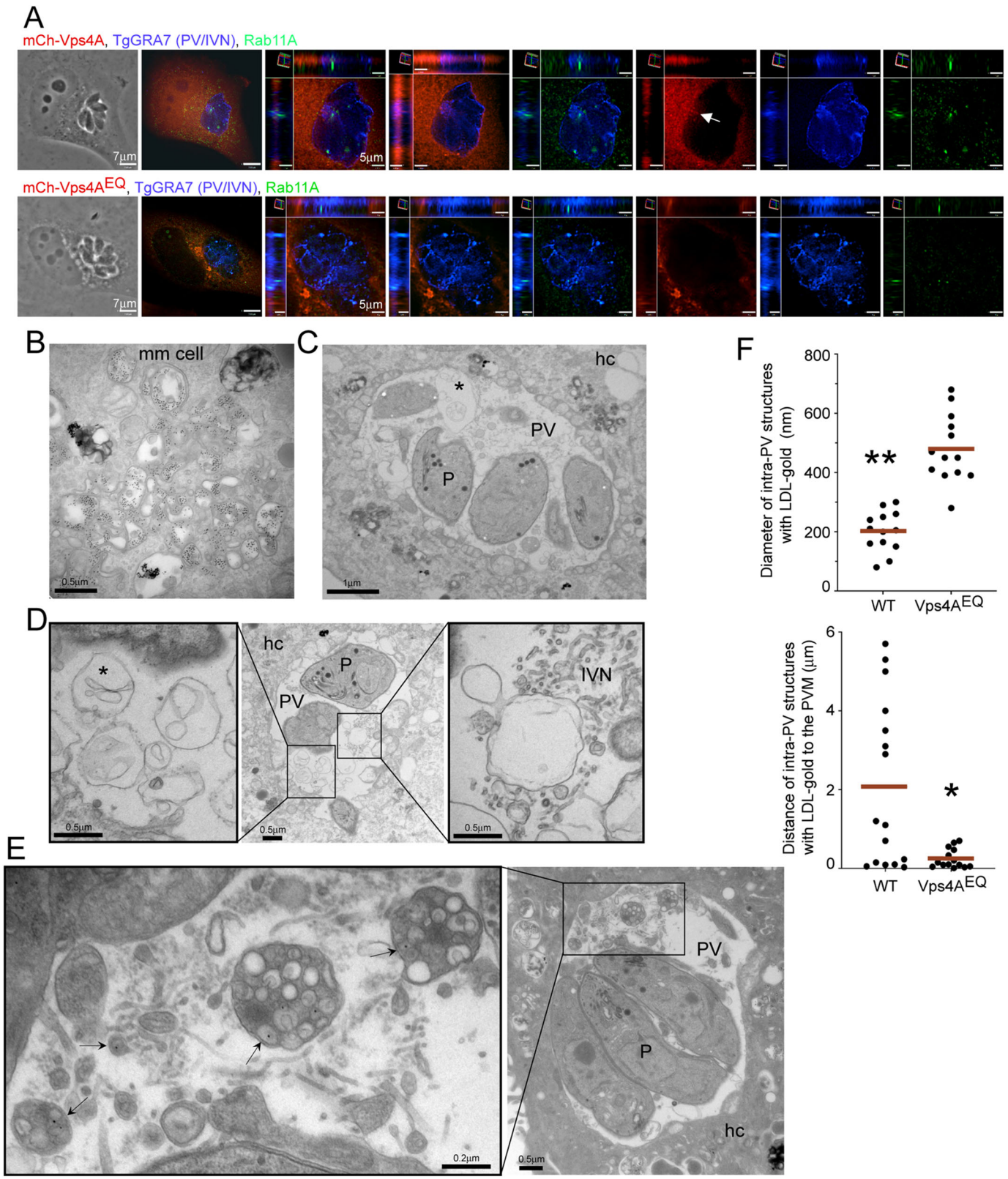

Fig. 5. See next page for legend.

role for TgGRA14 and TgGRA64, which both function to recruit host ESCRT components, in host vesicle uptake. It also emphasizes the foremost contribution of IVN tubules in entrapping host organelles.

DISCUSSION

Toxoplasma is proficient in manipulating its host cell to gain access to vital nutrients, either from the cytosol (e.g. molecules or proteins) or organelles (e.g. lipids). One strategy developed by

Journal of Cell Science (2023) 136, jcs260159. doi:10.1242/jcs.260159

Fig. 5. Effect of DN Vps4A on host organelle internalization. (A) IFA. HeLa cells were transiently transfected with either mCherry (mCh)–Vps4A^{WT} or mCherry-Vps4A^{EQ}. The cells were infected for 20 h, fixed and immunostained for TgGRA7 and Rab11A. Individual *z*-slices and cropped images of the PV (orthogonal views) shown. The arrow indicates PV-associated mCherry–Vps4A. (B–F) TEM. Infected HeLa cells expressing mCherry–Vps4A^{EQ} and incubated with LDL–gold particles show class E-like compartments containing gold particles in the host cytoplasm (B) and large membrane buds derived from the PVM (C,D, asterisks), some in contact with IVN tubules shown in D (right inset). In E, intra-PV detection of very large structures with accumulation of host LDL–gold organelles (arrows). hc, host cell; mm cell, mammalian cell; P, parasite. Images are representative of two independent experiments. (F) Measurement of the size and distance of intra-PV structures containing LDL–gold from their center to the PVM. Dot blots shown with red bars indicating the mean from one representative experiment. **P*=0.0032; ***P*<0.0001, (unpaired, two-tailed *t*-test). Intra-PV host organelle size and distance measurements were performed on 19–23 representative PV sections.

Toxoplasma for nutrient import is the formation of inward PVM buds, creating a pathway for host material into the PV. TEM examinations of the PVM illustrate various sizes and shapes (from vesicular to tubular) of PVM buds. We previously described two types of PVM invaginations that are depicted in our model in Fig. 8B: one generated by host microtubules recruited at the PV and poking into the PVM (Coppens et al., 2006), and the other mediated by IVN tubules secreted by *Toxoplasma* in the PV and fusing with the PVM (Romano et al., 2017). We also identified smaller PVM buds that were morphologically distinct from these two tubular PVM invaginations. Host endocytic structures are often observed encroached in these different PVM invaginations, before being engaged deeper into the PV lumen. ESCRT proteins remodel membranes by creating indentations and forming a bridge between membranes to enable fusion and fission. *Toxoplasma* expresses two proteins (TgGRA14 and TgGRA64) previously shown to interact with ESCRT machinery at the PVM

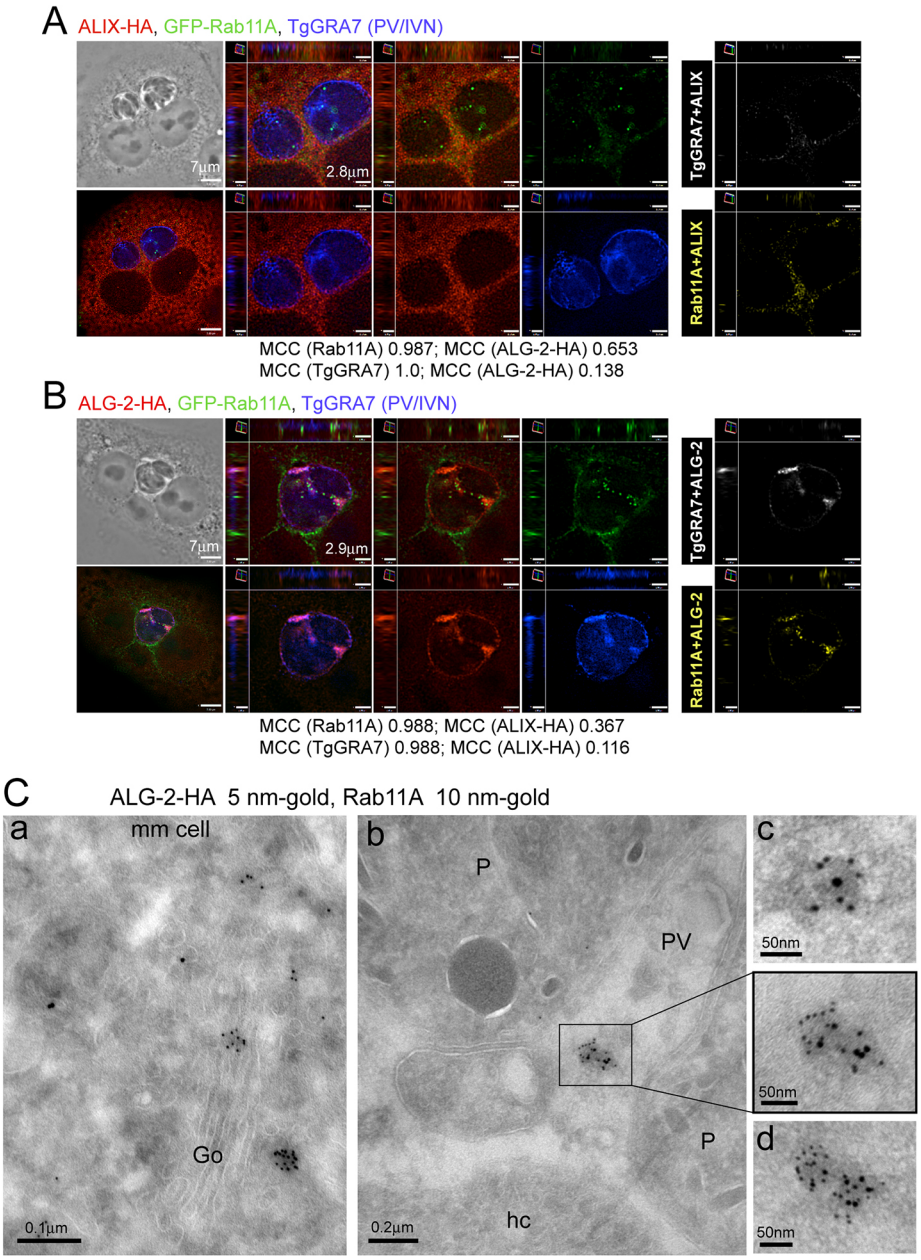

Fig. 6. Association of mammalian ALIX and ALG-2 with intra-PV Rab11A vesicles. (A,B). IFA. VERO cells stably expressing GFP–Rab11A were transfected with ALIX–HA (A) or ALG-2–HA (B), infected for 20 h, fixed and immunostained for HA and TgGRA7. Individual *z*-slices and cropped images of the PV (orthogonal views) are shown. In A, positive PDM images correlating ALIX–HA with GFP–Rab11A (yellow) and the PVM (GRA7) (white), and in B, positive PDM images correlating ALG-2–HA with GFP–Rab11A (yellow) or TgGRA7 (white) are shown. (C) Immune-EM. HeLa cells transfected with ALG-2–HA, infected for 20 h and fixed and processed for immuno-EM with anti-HA (5 nm gold particles) and anti-Rab11A (10 nm gold particles) antibodies. (a) ALG-2–HA and Rab11A in the mammalian (mm) cell. (b) Intra-PV structure with Rab11A membranes surrounded by ALG-2–HA (boxed region, with enlargement). (c,d) Additional representative images of intra-PV Rab11A vesicles surrounded by ALG-2–HA-containing membranes. Images are representative of 46 PVs analyzed in one experiment. Go, Golgi; P, parasite; hc, host cell.

Journal of Cell Science (2023) 136, jcs260159. doi:10.1242/jcs.260159

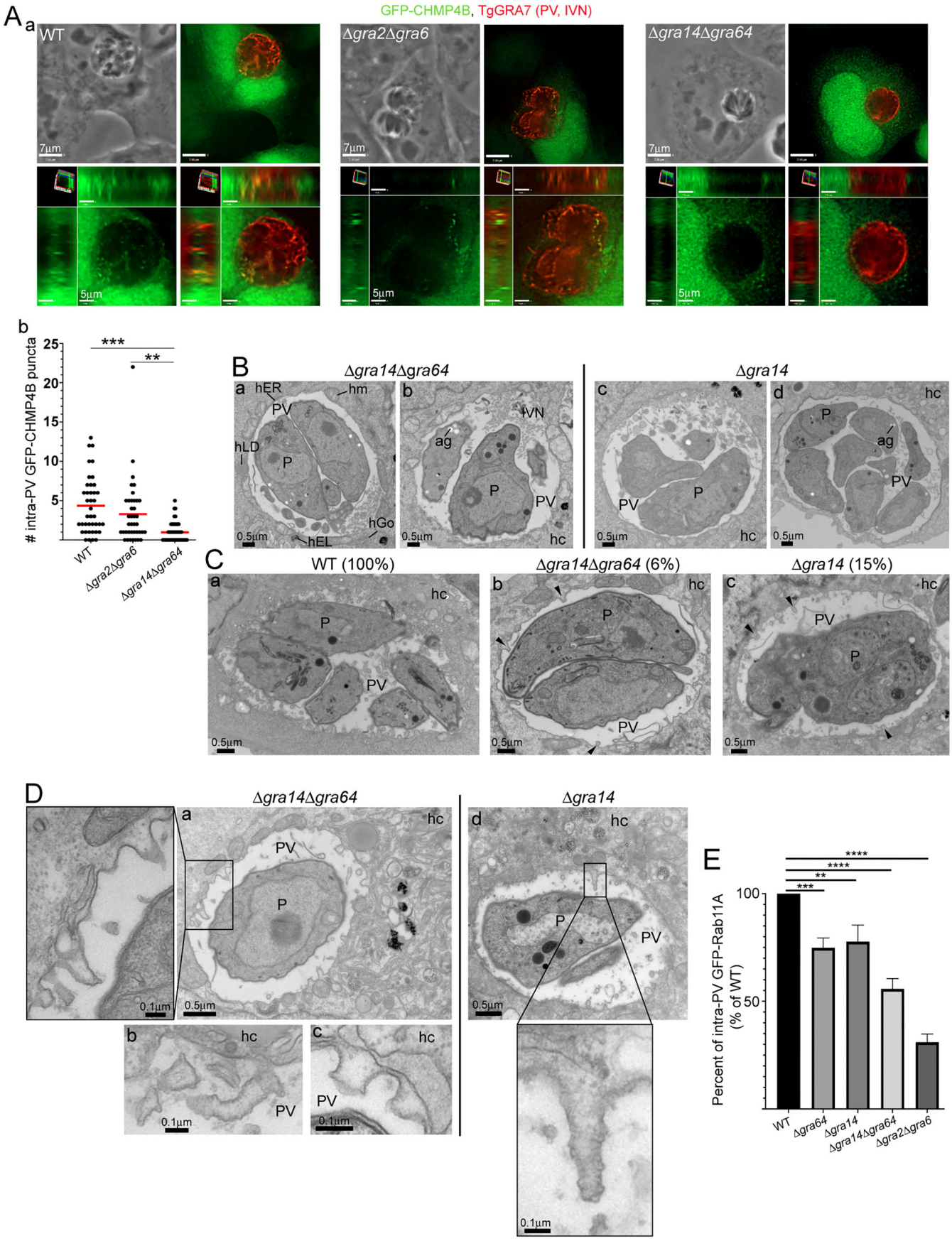

Fig. 7. See next page for legend.

Journal of Cell Science (2023) 136, jcs260159. doi:10.1242/jcs.260159

Fig. 7. Defects in Δ*gra14*, Δ*gra64* and Δ*gra14*Δ*gra64* parasites in PVM remodeling and Rab11A vesicle internalization. (A) IFA. HeLa cells stably expressing GFP–CHMP4B were infected with WT, Δ*gra2*Δ*gra6* or Δ*gra14*Δ*gra64* parasites for 20 h, fixed and immunostained for TgGRA7. (a) Individual *z*-slices and cropped images of the PV (orthogonal views) are shown. (b) The number of intra-PV GFP–CHMP4B puncta was measured for each mutant as described in the Materials and Methods. Dot plot from a representative experiment with mean (red bar) is shown. Numbers of PVs measured: WT, 40; Δ*gra2*Δ*gra6*, 39; and Δ*gra14*Δ*gra64*, 49. ***P*=0.002; *****P*<0.0001; one-way ANOVA with Tukey's multiple comparisons. (B–D) TEM. Non-transfected HeLa cells (B) or HeLa cells transfected with CHMP4B–mEm (C,D) were infected with WT, Δ*gra14*Δ*gra64* or Δ*gra14*Δ*gra64* parasites for 20 h and incubated with LDL–gold for ultrastructural analysis. Arrowheads in C point to short striated buds from the PVM of the mutants. The percentages represent the numbers of PV sections in which striated buds/invaginations were observed, divided by the total number of sections examined (66 for WT; 39 for Δ*gra14*; and 47 for Δ*gra14*Δ*gra64* parasites). ag, amylopectin granule; hc, host cell; hEL, host endolysosome; hER, host endoplasmic reticulum; hGo, host Golgi; hLD, host lipid droplet; hm, host mitochondrion; P, parasite. Images are representative of two independent experiments. (E) VERO cells stably expressing GFP–Rab11A were infected with WT or the indicated knockout mutant parasites for 20 h, fixed and immunostained with TgGRA7. The numbers of intra-PV Rab11A puncta were measured using Volocity. The mean number of intra-PV GFP–Rab11A puncta was calculated for each sample per experiment and converted into the percentage of WT puncta observed. Then, the mean±s.d. was calculated for three independent experiments and plotted. Number of PVs measured per experiment: WT (25, 26, 30); Δ*gra64* (28, 22, 25); Δ*gra14* (28, 25, 32); Δ*gra14*Δ*gra64* (24, 26, 30); Δ*gra2*Δ*gra6* (34, 26, 27). ***P*=0.0015; ****P*=0.0006, *****P*<0.0001; one-way ANOVA with Tukey's multiple comparisons.

and IVN (Rivera-Cuevas et al., 2021; Mayoral et al., 2022). In this study, we investigated how *Toxoplasma* exploits host ESCRT machinery by focusing on CHMP4B, ALIX, ALG-2 and Vps4A, for PVM budding and scission in relation to intra-PV sequestration of host endocytic organelles. On the parasite side, we examined the contribution of the two ESCRT interactors, TgGRA14 and TgGRA64. Based on our findings and published data (Romano et al., 2017; Rivera-Cuevas et al., 2021; Mayoral et al., 2022), we propose a model (Fig. 8C) summarizing the interplay between these host and parasite proteins for entrapping some host organelles into the PV.

ESCRT proteins govern membrane remodeling processes that require stabilizing membrane curvature, such as the formation of endosomal ILVs in MVBs (Vietri et al., 2020; Schöneberg et al., 2017; Pfitzner et al., 2021; Hurley, 2015). Similar to budding of the MVB limiting membrane, we propose that ESCRT components recruited to the PV generate PVM invaginations protruding into the PV lumen. At the PV, ESCRT-III proteins could oligomerize to form tight filamentous structures around the neck of the budding PVM and Vps4 ATP hydrolysis could provide the force necessary for pinching off PVM buds away from the host cytosol. Thus, formation of ILVs from the MVB membrane and intra-PV vesicles or tubules from the PVM might be viewed as topologically comparable. Under expression of the DN mutant Vps4A^{EQ}, very large membrane-bound compartments packed with many host endolysosomes were observed inside the PV, with a morphology distinct from structures typically found in the PV of WT cells, indicating that the lack of functional Vps4A interferes with proper internalization. The same phenotype was observed when FLAG–CHMP4B was overexpressed, with these large structures still connected to the PVM, suggesting impaired scission activity. Although the Vps4-binding domain is located near the C-terminal end of CHMP4B, it remains possible that the acidic FLAG tag interferes with the CHMP4B ANCHR domain that contributes to membrane binding, and might impede proper ESCRT-III association with membranes and Vps4 function.

Aspects of ESCRT-III recruitment, however, would differ from ILV biogenesis as it would involve parasite proteins. For example, a bioinformatics analysis identified TSG101- and ALIX-targeting motifs in TgGRA14, which are exposed to the host cytosol, and the Δ*gra14* mutant diminishes PVM recruitment of endogenously expressed GFP–TSG101 but has no effect on ALIX, suggesting the involvement of additional parasite proteins (Rivera-Cuevas et al., 2021). Using co-immunoprecipitation and proximity labeling, the parasite TgGRA64 protein was shown to interact with several host ESCRT components (CHMP4B, TSG101, ALG-2 and ALIX) (Mayoral et al., 2022). Our immunofluorescence assays show that the Δ*gra14*Δ*gra64* mutant still recruits CHMP4B at the PVM, indicating the expression of other ESCRT recruiters that compensate for the loss of *gra14* and *gra64*. Indeed, immunoprecipitation and proximity-labeling assays of TgGR14 or TgGRA64 have identified about 15 parasite proteins as potential candidates (Rivera-Cuevas et al., 2021) (Mayoral et al., 2022).

In *Toxoplasma*-infected epithelial cells, GFP–CHMP4B localizes to the host cytosol and nucleus with partial association of vesicles with the PVM and IVN. Puncta on the IVN suggest that CHMP4B-containing buds formed at the PVM are subsequently internalized into the PV at sites near the IVN. A recent publication on *Toxoplasma*-infected dendritic cells also revealed host CHMP4B at the PV, although in this cell line, CHMP4B relocalized almost completely to the PV, suggesting possible cell type variations (Croce et al., 2022). Overexpression of CHMP4B fused C-terminally with mEmerald generated impressive tubular PVM invaginations, enclosing CHMP4B spiral filaments. Membrane-associated ESCRT-III usually has a short lifespan (Baumgärtel et al., 2011; Jouvenet et al., 2011) owing to Vps4 activity in disassembling and recycling ESCRT-III subunits (Babst et al., 1998; Lin et al., 2005). Depletion of Vps4 can increase the lifetime of membrane-associated ESCRT-III, leading to the accumulation of plasma membrane ESCRT-III filaments that form uniform spiral assemblies with a mean outer diameter of 110 nm (Cashikar et al., 2014). Our DN CHMP4B–mEm system mimics Vps4 depletion, with the accumulation of stable PVM invaginations containing very long (up to 7 µm) and narrow (110 nm in diameter) CHMP4B filaments, reflecting a blockage of PVM scission. The stabilization of CHMP4B in its assembled state within PVM invaginations might be due to poor access of Vps4 to the MIT-interacting motif (MIM) domain of CHMP4B–mEm or insufficient amounts of Vps4 enzyme to depolymerize all the CHMP4B filaments at the PVM. The parasite proteins TgGRA14 and TgGRA64 could induce PVM invaginations through interaction with ESCRT components (e.g. CHMP4, TSG101 and ALIX) as fewer CHMP4B–mEm invaginations were detected by TEM in the Δ*gra14* mutant, with even fewer present in Δ*gra14*Δ*gra64*. Uniquely compared to other systems, CHMP4B-associated PVM buds or tubules seem to fuse with IVN tubules based on data showing sparse and short PVM invaginations in the Δ*gra2*Δ*gra6* mutant under DN CHMP4B–mEm expression. Through this fusion, additional membranes might be supplied, creating deeper invaginations in which host material could remained trapped, with no possible return to the host cell.

Journal of Cell Science (2023) 136, jcs260159. doi:10.1242/jcs.260159

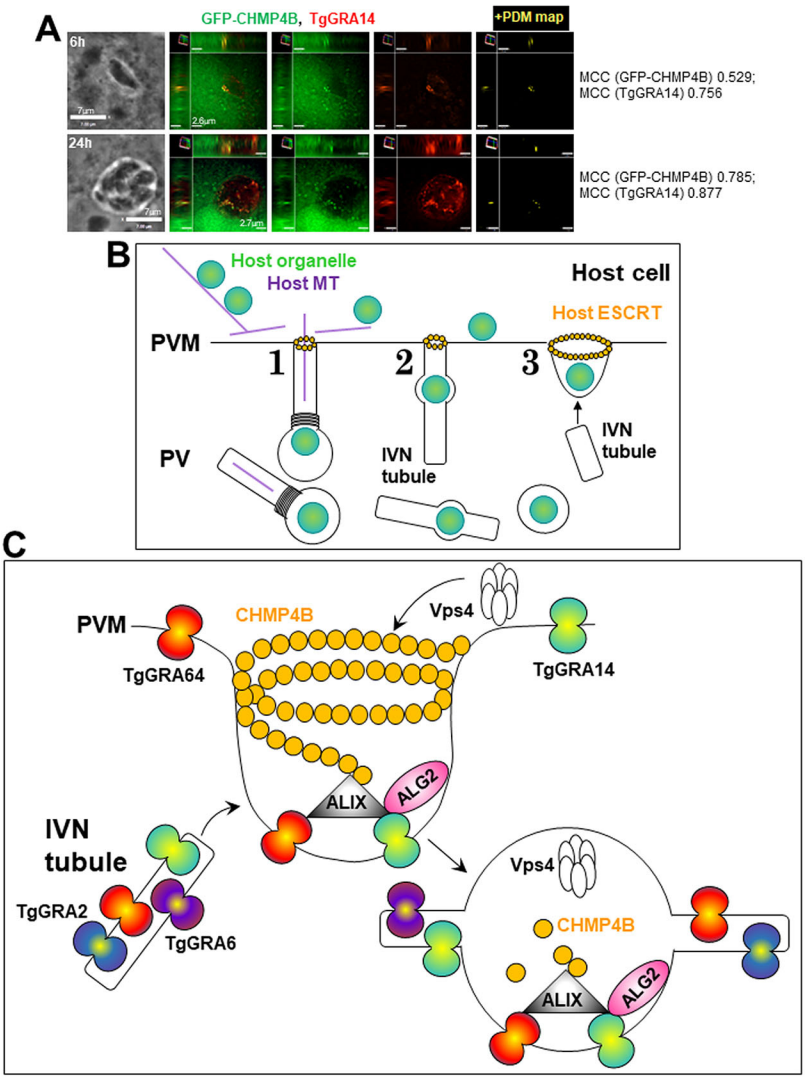

Fig. 8. TgGRA14 colocalization with GFP–CHMP4B and prospective model of host ESCRT-III components and Vps4 at the PV for internalization of the host organelle in synergy with the IVN. (A) IFA. HeLa cells stably expressing GFP–CHMP4B were infected for 6 or 24 h and immunostained for TgGRA7. Individual *z*-slices and cropped images of the PV (orthogonal views) are shown along with positive PDM images (yellow). Scale bars: 7 µm. (B) Overview of cellular events leading to host organelle trafficking along microtubules and internalization into the PV. Three PVM invaginations are depicted: (1) host microtubule (MT)-based invagination; (2) IVN tubule fused with the PVM; and (3) a bud with a broad neck. Host ESCRT-III components are recruited at the neck of these invaginations for detachment from the PVM. (C) Molecular players involved in host organelle internalization (host organelles not shown for clarity). TgGRA14 and TgGRA64 at the PV bind to ALIX interacting with CHMP4B subunits that cluster, resulting in deep membrane concavities with the walls of the membrane neck, close enough for fusion prior to Vps4 scission activity. Concomitantly, IVN tubules fuse with CHMP4B-induced tubules, contributing to their elongation and supply in membranes. Upon PVM detachment, tubulo-vesicles derived with PVM and IVN containing host organelles and residual ESCRT-III components and/or Vps4 accumulate inside the PV.

In summary, this study highlights unique features of ESCRT-mediated processes at the *Toxoplasma* PV. First, intravacuolar membranous tubules likely attach to ESCRT-mediated buds to elongate the invaginations at the PVM prior to scission. Second, ESCRT-mediated invaginations can be involved in the internalization of cargos as large as endosomes or Rab vesicles into the PV. Thus, the ESCRT machinery appears to function in a process more akin to phagocytosis for the engulfment of large particles. Lastly, many parasite proteins and perhaps distinct complexes might be involved in interfacing with host ESCRT at the PV. To this point, the Δ*gra14*Δ*gra64* mutant has a greater defect in host Rab11A vesicle internalization and in the formation of CHMP4B–mEm-induced PVM invaginations than single mutants, suggesting a synergistic role for TgGRA14 and TgGRA64 at the PVM/IVN through interactions with specific ESCRT components.

MATERIALS AND METHODS

Reagents and antibodies

All reagents were obtained from Sigma-Aldrich, unless otherwise stated. The following primary antibodies were used in this study: rat monoclonal and rabbit polyclonal anti-GRA7 (Coppens et al., 2006) and rabbit anti-GRA14 (graciously provided by Dr Yoshifumi Nishikawa, Obihiro University of Agriculture and Veterinary Medicine, Japan) (Ihara et al., 2020). Commercial antibodies include rabbit polyclonal anti-Rab11A (2413S, Cell Signaling Technology, Danvers, MA), rabbit polyclonal anti-GFP (A6455, Thermo Fisher Scientific), mouse monoclonal anti-HA.11 (clone 16B12, 901516; BioLegend, San Diego, CA) and mouse monoclonal anti-FLAG (clone M2, F1804; Sigma-Aldrich). The secondary antibodies used were: goat anti-rat, anti-rabbit and anti-mouse conjugated to Alexa Fluor 488, 594 or 350 (goat anti-rat IgG Alexa Fluor 488, A11006; goat anti-rat IgG Alexa Fluor 594, A11007; goat anti-rat IgG Alexa Fluor 350, A21093; goat anti-rabbit IgG Alexa Fluor 488, A11034; goat anti-rabbit IgG Alexa Fluor 594, A11037; goat anti-rabbit IgG Alexa Fluor 350, A21068; goat anti-mouse IgG Alexa Fluor 488, A11029; goat anti-mouse IgG Alexa Fluor 594, A11032; and goat anti-mouse IgG Alexa Fluor 350, A21049; Thermo Fisher Scientific).

Mammalian cell and parasite culture

Human foreskin fibroblasts (HFFs), HeLa and VERO cells were obtained from the American Type Culture Collection (Manassas, VA). VERO cells stably expressing GFP–Rab11A were described previously (Romano et al., 2017). HeLa cells stably expressing GFP–CHMP4B were generously provided by Dr Phyllis Hanson (University of Michigan, Ann Arbor, MI) (Jouvenet et al., 2011) and authenticated by siRNA against CHMP4B (Fig. S1A). All cells were grown in α-minimum essential medium (α-MEM) supplemented with 10% fetal bovine serum (FBS), 2 mM glutamine and penicillin/streptomycin (100 units/ml per 100 µg/ml) and maintained at 37°C in 5% CO_2 and checked for any contamination. The tachyzoite RH

Journal of Cell Science (2023) 136, jcs260159. doi:10.1242/jcs.260159

strain (type I lineage) of *Toxoplasma gondii* was used in this study. The RH strain deleted for both *gra2* and *gra6* (*Δgra2Δgra6*) was generously provided by Dr Marie-France Cesbron-Delauw (Université Grenoble Alpes, Grenoble, France) (Mercier et al., 2002). Generation of the RH *Δgra14* strain was described previously (Rivera-Cuevas et al., 2021). The RH *Δgra14Δgra64* strain (made in a *Δku80Δhxgprt* background for easier genetic manipulation) was generated identically to the *Δgra64* strains described in Mayoral et al. (2022). The *Δgra14Δgra64* strain was generated from the RH *Δgra64* strain as follows: first, CRISPR-Cas9 gene editing was used to target the endogenous *GRA14* locus by transfecting 7.5 µg of a vector expressing an HXGPRT resistance cassette and Cas9 with the guide RNA sequence 5′-CCAGAGACCAAGCGAATAGA-3′, along with 1.5 µg of a repair template generated by PCR (forward primer, 5′-TCCGAGTTTACACAGGCTGGGCTACCAGAGACCAAGCGAAGAACAGAAACTGATCTCAGA-3′; reverse primer, 5′-GGTTCCCGATTGGTCTACATTACTGACTTCAACCCTTCTAAAGATCCTCTTCGGAAATAA-3′), designed to insert three copies of the MYC epitope at the C-terminus of the gene for the purpose of confirming the absence of endogenous GRA14 protein after gene knockout. Following transfection, parasites were selected for in mycophenolic acid (25 µg/ml) and xanthine (50 µg/ml) for 1 week. Transfected parasites were subcloned by limiting dilution in 96-well plates. Successful tagging was demonstrated by IFA using the rabbit anti-MYC tag antibody (1:250; clone 71D10; 2278, Cell Signaling Technology) and by sequencing the PCR products amplified from genomic DNA by Sanger sequencing, using the following primers to amplify the C-terminus of GRA14: 5′-CGCCGAACCTGAACACAGAT-3′ and 5′-ATCACGCGTTCAATCACATC-3′. After generating a *Δgra64,GRA14-3×Myc* parasite strain, a CRISPR-Cas9 strategy was again used as described above, transfecting parasites with 7.5 µg of a Cas9 vector containing the guide RNA sequence 5′-GCGCGGGGGGACCGCTCGTC-3′ (targeting the *GRA14* start codon region) along with 280 pmol unannealed 100 bp donor oligos containing homologous arms and multiple stop codons in place of the endogenous GRA14 start codon (5′-CCACTGCTAAGCACAAAATGCAGGCGATAGCGCGGGGGGTAACTGACTGACTAGCTAACGGGACCGCTCGTCGGGGTGGTCGAGTTGTAGCTGGCTTTTC-3′, and the reverse complement of this sequence). Selection, subcloning and knockout screening was performed as described above, using the following primers to amplify the 5′UTR and N-terminus region of the *GRA14* locus to confirm the insertion of stop codons as designed: 5′-AGAAAGCGTCACTCAGACAT- 3′ and 5′-CTCCTAGATAGCTTACGGGC-3′. All parasites were propagated by serial passage in monolayers of HFFs (Roos et al., 1994; Khan and Grigg, 2017).

Plasmids

The plasmids used in this study include mEmerald-Mito-7 (Addgene plasmid #54160; deposited by Dr Michael Davidson); mEmerald-MAP4-C-10 (Addgene plasmid #54152; deposited by Dr Michael Davidson) (Planchon et al., 2011); plasmids encoding ALIX–HA and ALG-2–HA (generously provided by Dr John Boothroyd, Stanford University, Stanford, CA; Cygan et al., 2021), FLAG–CHMP4B (kindly provided by Dr Phyllis Hanson, University of Michigan, Ann Arbor, MI), mCherry–N1-VPS4A and mCherry–N1-VPS4A^{EQ} (graciously provided by Dr Akira Ono, University of Michigan, Ann Arbor, MI; Rivera-Cuevas et al., 2021); and pCHMP4B-mCherry (generously provided by Dr Jennifer Lippincott-Schwartz, Janelia Research Campus, Ashburn, VA; Elia et al., 2011).

To generate a plasmid with CHMP4B tagged at the 3′ end with mEmerald, we amplified CHMP4B from pCHMP4B-mCherry using the primers CHMP4B_Cterm forward (5′-ATCCGCTAGCATGTCGGTGTTCGGGAAG-3′) and CHMP4B_C-term reverse (5′-GTGGATCCCCCATGGATCCAGCCCAGTTC-3′), and we amplified the sequence including mEmerald but omitting the mitochondrial-targeting sequence from the mEmerald-Mito-7 plasmid using the primers mEmeraldVector forward (5′-TGGATCCATGGGGGATCCACCGGTCGCC-3′) and mEmeraldVector reverse (5′-ACACCGACATGCTAGCGGATCTGACGGTTCAC-3′). We then combined these fragments using the HiFi assembly kit (New England Biolabs, Ipswich, MA) to create a plasmid expressing CHMP4B–mEm, with a 7 amino acid linker between CHMP4B and mEmerald. To generate a plasmid with CHMP4B tagged at the 5′ end with mEmerald, we amplified CHMP4B from pCHMP4B-mCherry using the primers NlinkCHMP4B_fwd (5′-GCTGTACAAGTCCGGACTCAGATCT-3′) and NlinkCHMP4B_rev (5′-CGGTGGATCCTTACATGGATCCAGCCCAG-3′); mEmerald from mEmerald-MAP4-C-10 using the primers N_Emerald_fwd (5′-GGTCGCCACCATGGTGAGCAAGGGCGAG-3′) and N_Emerald_rev (5′-TGAGTCCG GACTTGTACAGCTCGTCCATGC-3′); and the vector sequence from mEmerald-MAP4-C-10 using mEmMAPVector_fwd (5′-ATCCATGTAAGGATCCACCGGATCTAGATAACTGATCATAATCAGC-3′) and mEmMAPVector_rev (5′-TGCTCACCATGGTGGCGACCGGTAGCGC-3′). We then combined the fragments using the HiFi assembly kit to create a plasmid expressing mEm–CHMP4B, with a 12 amino acid linker between mEmerald and CHMP4B.

LDL–gold preparation

Human LDL was isolated from fresh serum by zonal density gradient ultracentrifugation as described previously (Poumay and Ronveaux-Dupal, 1985). Briefly, the density of human serum was increased to 1.25 g/ml with KBr, centrifuged at 81,900 ***g*** (MLA-80 rotor; Beckman Instruments, Palo Alto, CA) for 24 h at 4°C. The supernatant (lipoproteins) was collected, adjusted to a density of 0.126 g/ml, placed in the bottom of a centrifuge tube and layered on top with 0.9% NaCl (1:5 v/v). After ultracentrifugation at 81,900 ***g*** for 6 h at 4°C, LDL (middle, yellow layer) was collected, extensively dialyzed against 2 mM sodium borate pH 9, and filtered with a 0.2 µm PVDF syringe filter and stored at 4°C. For the coupling reaction of LDL to gold particles of 15 nm in diameter, a solution of 0.3 mM tetrachloroauric acid was reduced with 1.16 mM sodium citrate, as described previously (De Roe et al., 1987), except for the addition of 0.00015% tannic acid for gold stabilization under boiling until the mixture became dark red. For LDL–gold complex preparation, a solution of LDL adjusted at 0.2 mg/ml was added to a solution of gold particles at 57 µg/ml (1:5 v/v) for 30 min with gentle agitation, before addition of 1 ml of 1% bovine serum albumin in 2 mM sodium borate pH 9. After 5 min, 5 ml of LDL–gold conjugate was layered on 1 ml of a 1.15 M sucrose cushion and sedimented at 97,500 ***g*** using a Beckman T150 rotor. The solution of LDL–gold conjugates collected from the sucrose solution was dialyzed against PBS before use.

Transfection and parasite infection

For fluorescence microscopy, HeLa cells were transiently transfected using jetPRIME (Polyplus, Illkirch, France) according to the manufacturer's instructions. HeLa cells (~50,000) were seeded to coverslips the day before transfection. For the transfection, 0.2 µg DNA in 50 µl jetPRIME buffer was mixed with 0.4 µl jetPRIME reagent and incubated at room temperature for 10 min prior to addition to cells. VERO cells expressing GFP–Rab11A (~40,000) were seeded to coverslips the day before transfection. For the transfection, 0.8 µg of DNA in 50 µl jetOPTIMUS buffer (Polyplus) was mixed with 0.75 µl jetOPTIMUS reagent and incubated at room temperature for 10 min prior to addition to the cells. For TEM, HeLa cells were grown in six-well plates to 60% confluency, and plasmid DNA (1 µg per well) was mixed with jetOPTIMUS reagent (1 µl per well) and incubated at room temperature for 10 min according to the manufacturer's instructions (Polyplus), before being added to the cells. All transfected cells were incubated at 37°C with 5% CO_2 for 4 h, washed with PBS, and allowed to recover for 1 h at 37°C with 5% CO_2 prior to infection with parasites. For infection, freshly egressed parasites were added to the cells for 1 h, washed with PBS to remove extracellular parasites and incubated for the times indicated in α-MEM. For some samples, LDL complexed with gold was added in α-MEM medium with 10% (v/v) of delipidated FBS (Cocalico Biologicals, Stevens, PA) and the cells were incubated at 37°C in 5% CO_2 for 20 h. Infected cells were fixed for either fluorescence microscopy or TEM.

siRNA

HeLa cells stably expressing GFP–CHMP4B were seeded to coverslips and grown to 50% confluency. The cells were transfected using jetPRIME according to the manufacturer's instructions with siRNA control (ON-TARGET plus non-targeting pool, 5 nmol; D-001810-10-05; Dharmacon/Horizon Discovery, Waterbeach, UK) or CHMP4B siRNA [ON-TARGET

Journal of Cell Science (2023) 136, jcs260159. doi:10.1242/jcs.260159

plus human CHMP4B (128866), SMART pool, 5 nmol; L-018075-01-0005; Dharmacon/Horizon Discovery] using 27.5 pmol of siRNA. Samples were fixed at 24, 48 and 72 h post transfection and mounted with ProLong Glass mounting medium.

Cell labeling

For immunolabeling, cells were fixed in PBS with 4% formaldehyde (Polysciences) and 0.02% glutaraldehyde for 15 min. Cells were permeabilized with 0.3% Triton X-100 in PBS for 5 min and washed twice with PBS before blocking. Cells were incubated in blocking buffer (3% bovine serum albumin, fraction V; Thermo Fisher Scientific) in PBS for 1 h, followed by incubation in primary antibodies diluted in blocking buffer (1:800 for anti-GRA7; 1:1000 for anti-HA; 1:1500 for anti-FLAG; 1:100 for anti-Rab11A; 1:500 for anti-GRA14) for 1 h or overnight (anti-Rab11A only). Cells were washed three times with PBS for 5 min each and then incubated in secondary antibodies diluted (1:2000) in blocking buffer for 45 min to 1 h, followed by three washes with PBS for 5 min each. In some cases, cells were incubated with a 1:1000 dilution of 1 mg/ml DAPI (Roche Diagnostics) in PBS for 5 min, followed by three washes with PBS. Coverslips were rinsed with water and mounted on slides with ProLong Diamond mounting solution.

Fluorescence microscopy

Fixed samples were viewed with a Zeiss AxioImager M2 fluorescence microscope equipped with an oil-immersion Zeiss plan Apo 100×/NA 1.4 objective or a Zeiss EC plan Neo 40×/NA 0.75 objective (siRNA samples) and a Hamamatsu ORCA-R2 camera. Optical *z*-sections with 0.2 µm spacing were acquired using Volocity software (Quorum Technologies, Puslinch, ON, Canada). For siRNA samples, only a single *z*-plane was acquired.

Image analysis

Images were deconvolved with an iterative restoration algorithm using calculated point-spread functions, a confidence limit of 100% and iteration limit of 30–35 using Volocity software. Images were cropped and adjusted for brightness and contrast using Volocity software. Figures were compiled in Adobe Illustrator.

To characterize the intra-PV GFP–Rab11A foci, we acquired optical *z*-sections of infected cells with PV containing eight parasites to normalize for PV size. After deconvolution, images were analyzed with a measurement protocol generated in Volocity (Quorum Technologies) according to published protocols with some modifications (Romano et al., 2017, 2021). The measurement protocol measured objects in 3D-reconstructed volumes of optical *z*-slices. The PV was identified by the fluorescence intensity of TgGRA7 signal; thresholds were set manually by using the outer TgGRA7 PVM staining as the boundary of the PV, and the minimum object size was set to 20 μm^3. To close any holes in the identified structure, the close function was used with 20 iterations. GFP–Rab11A puncta were identified by fluorescence intensity (automatic thresholds with an offset threshold ranging from 110–170%, minimum object size of 0.4 μm^3), noise was removed using a medium filter, and objects were separated using the 'separate touching objects' tool in Volocity with an object size guide of 0.1 μm^3. Lastly, the 'compartmentalize' function in Volocity was used to identify GFP–Rab11A objects inside the PV. The number and volume of GFP–Rab11A puncta inside the PV were calculated plus the distance of the intra-PV GFP–Rab11A puncta to the PV centroid.

To assess the number of GFP–CHMP4B puncta associated with the PV, optical *z*-sections of infected cells were acquired, deconvolved and measured using the following measurement protocols in Volocity: the PV was identified with the 'Find Objects Measurement' tool using TgGRA7 fluorescence with automatic thresholding and a minimum object size of 10 μm^3. Next, GFP–CHMP4B was identified with the 'Find Objects Measurement' tool based on GFP fluorescence with thresholding using standard deviation intensity (lower limit of 1) and a minimum object size of 0.1 μm^3. Lastly, the 'Compartmentalize' tool was used to determine the number of GFP–CHMP4B puncta inside the PV.

MCCs were calculated using Volocity software along with a product of the difference of the means map (PDM), which is generated by identifying voxels where each signal is above its mean value after thresholding for background. Thresholds were set by measuring, using a region of interest (ROI), the fluorescence intensity of each channel in a region of the nucleus without staining for either signal (background) (Fig. S2). In all other instances, thresholds were set by measuring, using an ROI, the fluorescence intensity of each channel in a region between cells. These background values (per image) were used to calculate MCC and PDM values of the corresponding individual infected cells. The positive PDM shows voxels where both fluorescence signals are above the mean and show positive correlation.

For each siRNA sample, 15 random fields were captured as a single *z*-plane. To measure fluorescence intensity, an ROI encompassing the entire field was drawn and the mean fluorescence intensity was measured using Volocity software. Intensity values were plotted using GraphPad Prism (San Diego, CA).

TEM

For thin-section TEM, cells were fixed in 2.5% glutaraldehyde (Electron Microscopy Sciences, Hatfield, PA) in 0.1 M sodium cacodylate buffer (pH 7.4) for 1 h at room temperature and processed as described previously (Fölsch et al., 2001).

For immunogold staining, cells were fixed in 4% paraformaldehyde (Electron Microscopy Sciences) in 0.25 M HEPES (pH 7.4) for 1 h at room temperature, and then in 8% paraformaldehyde in the same buffer overnight at 4°C. They were infiltrated, frozen and sectioned as described previously (Romano et al., 2017). The sections were immunolabeled with antibodies against GFP at a 1:10 dilution, HA at a 1:50 dilution or Rab11A at a 1:10 dilution in PBS containing 1% fish skin gelatin, and then with secondary IgG antibodies coupled to 10 nm protein A-gold particles, before examination with a Philips CM120 electron microscope or a Hitachi 7600 electron microscope under 80 kV, equipped with a dual AMT CCD camera system. The AMT v6.1 software was used for quantitative measurement of the diameter of PVM invaginations with CHMP4B–mEm (from 62 invaginations from 26 different PV sections) and of intra-PV host organelle size and distance performed on 19–23 representative PV sections.

Statistical analysis

Numerical data are presented as mean±s.d. or in dot plots with means indicated (GraphPad Prism). To compare samples, we used a one-way ANOVA with a Tukey's multiple comparisons test or unpaired two-tailed *t*-tests using GraphPad Prism.

Acknowledgements

We thank the members of the Coppens laboratory for helpful discussion during the course of this work, and especially Karen Ehrenman for her help in cloning the mEmerald–CHMP4B and CHMP4B–mEmerald plasmids. We are grateful to Phyllis Hanson for helpful advice and discussions related to this work. We also thank the generous providers of plasmids and parasite strains used in this study. We thank the excellent technical staff from Electron Microscopy Core facilities at Johns Hopkins University School of Medicine (M. Delannoy and B. Smith) and Yale University School of Medicine (K. Zichichi).

Competing interests

The authors declare no competing or financial interests.

Author contributions

Conceptualization: J.D.R., I.C., J.M., L.M.W., V.B.C.; Methodology: J.D.R., I.C., J.M., R.B.G.; Validation: J.D.R., I.C.; Formal analysis: J.D.R., I.C.; Investigation: I.C., J.D.R.; Resources: J.D.R., I.C., J.M., R.B.G., Y.R.-C.; Data curation: J.D.R., I.C.; Writing – original draft: J.D.R., I.C.; Writing – review & editing: J.D.R., I.C., J.M., R.B.G., Y.R.-C., L.M.W., V.B.C.; Visualization: J.D.R., I.C.; Funding acquisition: I.C.

Funding

This study was supported by grants from the National Institutes of Health (R01 AI060767 to I.C. and R01 AI134753 to L.M.W.). Deposited in PMC for release after 12 months.

Data availability

All relevant data can be found within the article and its supplementary information.

First Person

This article has an associated First Person interview with the first author of the paper.

Peer review history

The peer review history is available online at https://journals.biologists.com/jcs/article-lookup/doi/10.1242/jcs.260159.reviewer-comments.pdf

References

Alonso Y. Adell, M., Migliano, S. M. and Teis, D. (2016). ESCRT-III and Vps4: a dynamic multipurpose tool for membrane budding and scission. *FEBS J.* **283**, 3288-3302. doi:10.1111/febs.13688

Babst, M., Wendland, B., Estepa, E. J. and Emr, S. D. (1998). The Vps4p AAA ATPase regulates membrane association of a Vps protein complex required for normal endosome function. *EMBO J.* **17**, 2982-2993. doi:10.1093/emboj/17.11.2982

Baumgärtel, V., Ivanchenko, S., Dupont, A., Sergeev, M., Wiseman, P. W., Kräusslich, H.-G., Bräuchle, C., Müller, B. and Lamb, D. C. (2011). Live-cell visualization of dynamics of HIV budding site interactions with an ESCRT component. *Nat. Cell Biol.* **13**, 469-474. doi:10.1038/ncb2215

Bishop, N. and Woodman, P. (2000). ATPase-defective Mammalian VPS4 localizes to aberrant endosomes and impairs cholesterol trafficking. *Mol. Biol. Cell* **11**, 227-239. doi:10.1091/mbc.11.1.227

Bittame, A., Effantin, G., Pètre, G., Ruffiot, P., Travier, L., Schoehn, G., Weissenhorn, W., Cesbron-Delauw, M.-F., Gagnon, J. and Mercier, C. (2015). *Toxoplasma gondii*: biochemical and biophysical characterization of recombinant soluble dense granule proteins GRA2 and GRA6. *Biochem. Biophys. Res. Commun.* **459**, 107-112. doi:10.1016/j.bbrc.2015.02.078

Cashikar, A. G., Shim, S., Roth, R., Maldazys, M. R., Heuser, J. E. and Hanson, P. I. (2014). Structure of cellular ESCRT-III spirals and their relationship to HIV budding. *Elife* **3**, e02184. doi:10.7554/eLife.02184

Coppens, I., Dunn, J. D., Romano, J. D., Pypaert, M., Zhang, H., Boothroyd, J. C. and Joiner, K. A. (2006). *Toxoplasma gondii* sequesters lysosomes from mammalian hosts in the vacuolar space. *Cell* **125**, 261-274. doi:10.1016/j.cell.2006.01.056

Coppin, A., Dzierszinski, F., Legrand, S., Mortuaire, M., Ferguson, D. and Tomavo, S. (2003). Developmentally regulated biosynthesis of carbohydrate and storage polysaccharide during differentiation and tissue cyst formation in *Toxoplasma gondii*. *Biochimie* **85**, 353-361. doi:10.1016/S0300-9084(03)00076-2

Croce, C., Garrido, F., Dinamarca, S., Santi-Rocca, J., Marion, S., Blanchard, N., Mayorga, L. S. and Cesbrian, I. (2022). Efficient cholesterol transport in dendritic cells defines optimal exogenous antigen presentation and *Toxoplasma gondii* proliferation. *Front. Cell Dev. Biol.* **10**, 837574. doi:10.3389/fcell.2022.837574

Cygan, A. M., Beltran, P. M. J., Mendoza, A. G., Branon, T. C., Ting, A. Y., Carr, S. A. and Boothroyd, J. C. (2021). Proximity-labeling reveals novel host and parasite proteins at the *Toxoplasma* parasitophorous vacuole membrane. *mBio* **12**, e0026021. doi:10.1128/mBio.00260-21

De Melo, E. J. T., De Carvalho, T. U. and De Souza, W. (1992). Penetration of *Toxoplasma gondii* into host cells induces changes in the distribution of the mitochondria and the endoplasmic reticulum. *Cell Struct. Funct.* **17**, 311-317. doi:10.1247/csf.17.311

De Roe, C., Courtoy, P. J. and Baudhuin, P. (1987). A model of protein-colloidal gold interactions. *J. Histochem. Cytochem.* **35**, 1191-1198. doi:10.1177/35.11.3655323

De Souza, W. and Attias, M. (2015). New views of the *Toxoplasma gondii* parasitophorous vacuole as revealed by Helium Ion Microscopy (HIM). *J. Struct. Biol.* **191**, 76-85. doi:10.1016/j.jsb.2015.05.003

Dou, Z., Mcgovern, O. L., Di Cristina, M. and Carruthers, V. B. (2014). *Toxoplasma gondii* ingests and digests host cytosolic proteins. *mBio* **5**, e01188-14. doi:10.1128/mBio.01188-14

Elia, N., Sougrat, R., Spurlin, T. A., Hurley, J. H. and Lippincott-Schwartz, J. (2011). Dynamics of endosomal sorting complex required for transport (ESCRT) machinery during cytokinesis and its role in abscission. *Proc. Natl. Acad. Sci. USA* **108**, 4846-4851. doi:10.1073/pnas.1102714108

Fölsch, H., Pypaert, M., Schu, P. and Mellman, I. (2001). Distribution and function of Ap-1 clathrin adaptor complexes in polarized epithelial cells. *J. Cell Biol.* **152**, 595-606. doi:10.1083/jcb.152.3.595

Griffith, M. B., Pearce, C. S. and Heaslip, A. T. (2022). Dense granule biogenesis, secretion, and function in *Toxoplasma gondii*. *J. Eukaryot Microbiol.* **69**, e12904. doi:10.1111/jeu.12904

Guérin, A., Corrales, R. M., Parker, M. L., Lamarque, M. H., Jacot, D., El Hajj, H., Soldati-Favre, D., Boulanger, M. J. and Lebrun, M. (2017). Efficient invasion by *Toxoplasma* depends on the subversion of host protein networks. *Nat. Microbiol.* **2**, 1358-1366. doi:10.1038/s41564-017-0018-1

Harker-Kirschneck, L., Baum, B. and Šarić, A. (2019). Changes in ESCRT-III filament geometry drive membrane remodelling and fission in silico. *BMC Biol.* **17**, 82. doi:10.1186/s12915-019-0700-2

Hartman, E. J., Asady, B., Romano, J. D. and Coppens, I. (2022). The Rab11-Family Interacting Proteins reveal selective interaction of mammalian recycling endosomes with the *Toxoplasma* parasitophorous vacuole in a Rab11- and Arf6-dependent manner. *Mol. Biol. Cell.* **33**, ar34. doi:10.1091/mbc.E21-06-0284

Henne, W. M., Buchkovich, N. J., Zhao, Y. and Emr, S. D. (2012). The endosomal sorting complex ESCRT-II mediates the assembly and architecture of ESCRT-III helices. *Cell* **151**, 356-371. doi:10.1016/j.cell.2012.08.039

Howard, T. L., Stauffer, D. R., Degnin, C. R. and Hollenberg, S. M. (2001). CHMP1 functions as a member of a newly defined family of vesicle trafficking proteins. *J. Cell Sci.* **114**, 2395-2404. doi:10.1242/jcs.114.13.2395

Hurley, J. H. (2015). ESCRTs are everywhere. *EMBO J.* **34**, 2398-2407. doi:10.15252/embj.201592484

Ihara, F., Fereig, R. M., Himori, Y., Kameyama, K., Umeda, K., Tanaka, S., Ikeda, R., Yamamoto, M. and Nishikawa, Y. (2020). *Toxoplasma gondii* dense granule proteins 7, 14, and 15 are involved in modification and control of the immune response mediated via NF-κB Pathway. *Front. Immunol.* **11**, 1709. doi:10.3389/fimmu.2020.01709

Jouvenet, N., Zhadina, M., Bieniasz, P. D. and Simon, S. M. (2011). Dynamics of ESCRT protein recruitment during retroviral assembly. *Nat. Cell Biol.* **13**, 394-401. doi:10.1038/ncb2207

Katoh, K., Shibata, H., Suzuki, H., Nara, A., Ishidoh, K., Kominami, E., Yoshimori, T. and Maki, M. (2003). The ALG-2-interacting protein Alix associates with CHMP4b, a human homologue of yeast Snf7 that is involved in multivesicular body sorting. *J. Biol. Chem.* **278**, 39104-39113. doi:10.1074/jbc.M301604200

Khan, A. and Grigg, M. E. (2017). *Toxoplasma gondii*: laboratory maintenance and growth. *Curr. Protoc. Microbiol.* **44**, 20C.1.1-20C.1.17. doi:10.1002/cpmc.26

Lata, S., Roessle, M., Solomons, J., Jamin, M., Gőttlinger, H. G., Svergun, D. I. and Weissenhorn, W. (2008). Structural basis for auto-inhibition of ESCRT-III CHMP3. *J. Mol. Biol.* **378**, 818-827. doi:10.1016/j.jmb.2008.03.030

Lin, Y., Kimpler, L. A., Naismith, T. V., Lauer, J. M. and Hanson, P. I. (2005). Interaction of the mammalian endosomal sorting complex required for transport (ESCRT) III protein hSnf7-1 with itself, membranes, and the AAA+ ATPase SKD1. *J. Biol. Chem.* **280**, 12799-12809. doi:10.1074/jbc.M413968200

Magno, R. C., Lemgruber, L., Vommaro, R. C., De Souza, W. and Attias, M. (2005). Intravacuolar network may act as a mechanical support for *Toxoplasma gondii* inside the parasitophorous vacuole. *Microsc. Res. Tech.* **67**, 45-52. doi:10.1002/jemt.20182

Martin-Serrano, J., Yaravoy, A., Perez-Caballero, D. and Bieniasz, P. D. (2003). Divergent retroviral late-budding domains recruit vacuolar protein sorting factors by using alternative adaptor proteins. *Proc. Natl. Acad. Sci. USA* **100**, 12414-12419. doi:10.1073/pnas.2133846100

Maxfield, F. R. and Mcgraw, T. E. (2004). Endocytic recycling. *Nat. Rev. Mol. Cell Biol.* **5**, 121-132. doi:10.1038/nrm1315

Mayoral, J., Guevara, R. B., Rivera-Cuevas, Y., Tu, V., Tomita, T., Romano, J. D., Gunther-Cummins, L., Sidoli, S., Coppens, I., Carruthers, V. B. et al. (2022). Dense granule protein, GRA64 interacts with host cell ESCRT proteins during *Toxoplasma gondii* infection. *mBio* **13**, e0144222. doi:10.1128/mbio.01442-22

Mccullough, J., Fisher, R. D., Whitby, F. G., Sundquist, W. I. and Hill, C. P. (2008). ALIX-CHMP4 interactions in the human ESCRT pathway. *Proc. Natl. Acad. Sci. USA* **105**, 7687-7691. doi:10.1073/pnas.0801567105

Mccullough, J., Clippinger, A. K., Talledge, N., Skowyra, M. L., Saunders, M. G., Naismith, T. V., Colf, L. A., Afonine, P., Arthur, C., Sundquist, W. I. et al. (2015). Structure and membrane remodeling activity of ESCRT-III helical polymers. *Science* **350**, 1548-1551. doi:10.1126/science.aad8305

Melo, E. J. T. and De Souza, W. (1997). Relationship between the host cell endoplasmic reticulum and the parasitophorous vacuole containing *Toxoplasma gondii*. *Cell Struct. Func.* **22**, 317-323. doi:10.1247/csf.22.317

Mercier, C. and Cesbron-Delauw, M.-F. (2015). *Toxoplasma* secretory granules: one population or more? *Trends Parasitol.* **31**, 60-71. doi:10.1016/j.pt.2014.12.002

Mercier, C., Dubremetz, J.-F., Rauscher, B., Lecordier, L., Sibley, L. D. and Cesbron-Delauw, M.-F. (2002). Biogenesis of nanotubular network in *Toxoplasma* parasitophorous vacuole induced by parasite proteins. *Mol. Biol. Cell* **13**, 2397-2409. doi:10.1091/mbc.e02-01-0021

Muzioł, T., Pineda-Molina, E., Ravelli, R. B., Zamborlini, A., Usami, Y., Göttlinger, H. and Weissenhorn, W. (2006). Structural basis for budding by the ESCRT-III factor CHMP3. *Dev. Cell* **10**, 821-830. doi:10.1016/j.devcel.2006.03.013

Obita, T., Saksena, S., Ghazi-Tabatabai, S., Gill, D. J., Perisic, O., Emr, S. D. and Williams, R. L. (2007). Structural basis for selective recognition of ESCRT-III by the AAA ATPase Vps4. *Nature* **449**, 735-739. doi:10.1038/nature06171

Panas, M. W. and Boothroyd, J. C. (2021). Seizing control: how dense granule effector proteins enable *Toxoplasma* to take charge. *Mol. Microbiol.* **115**, 466-477. doi:10.1111/mmi.14679

Pernas, L. and Boothroyd, J. C. (2010). Association of host mitochondria with the parasitophorous vacuole during *Toxoplasma* infection is not dependent on rhoptry

proteins ROP2/8. *Int. J. Parasitol.* **40**, 1367-1371. doi:10.1016/j.ijpara.2010.07.002

Pernas, L., Adomako-Ankomah, Y., Shastri, A. J., Ewald, S. E., Treeck, M., Boyle, J. P. and Boothroyd, J. C. (2014). *Toxoplasma* effector MAF1 mediates recruitment of host mitochondria and impacts the host response. *PLoS Biol.* **12**, e1001845. doi:10.1371/journal.pbio.1001845

Pfitzner, A.-K., Moser Von Filseck, J. and Roux, A. (2021). Principles of membrane remodeling by dynamic ESCRT-III polymers. *Trends Cell Biol.* **31**, 856-868. doi:10.1016/j.tcb.2021.04.005

Piper, R. C. and Katzmann, D. J. (2007). Biogenesis and function of multivesicular bodies. *Annu. Rev. Cell Dev. Biol.* **23**, 519-547. doi:10.1146/annurev.cellbio.23.090506.123319

Planchon, T. A., Gao, L., Milkie, D. E., Davidson, M. W., Galbraith, J. A., Galbraith, C. G. and Betzig, E. (2011). Rapid three-dimensional isotropic imaging of living cells using Bessel beam plane illumination. *Nat. Methods* **8**, 417-423. doi:10.1038/nmeth.1586

Poumay, Y. and Ronveaux-Dupal, M. F. (1985). Rapid preparative isolation of concentrated low density lipoproteins and of lipoprotein-deficient serum using vertical rotor gradient ultracentrifugation. *J. Lipid Res.* **26**, 1476-1480. doi:10.1016/S0022-2275(20)34253-X

Pszenny, V., Ehrenman, K., Romano, J. D., Kennard, A., Schultz, A., Roos, D. S., Grigg, M. E., Carruthers, V. B. and Coppens, I. (2016). A lipolytic lecithin: cholesterol acyltransferase secreted by *Toxoplasma* facilitates parasite replication and egress. *J. Biol. Chem.* **291**, 3725-3746. doi:10.1074/jbc.M115.671974

Rivera-Cuevas, Y., Mayoral, J., Di Cristina, M., Lawrence, A.-L. E., Olafsson, E. B., Patel, R. K., Thornhill, D., Waldman, B. S., Ono, A., Sexton, J. Z. et al. (2021). *Toxoplasma gondii* exploits the host ESCRT machinery for parasite uptake of host cytosolic proteins. *PLoS Pathog.* **17**, e1010138. doi:10.1371/journal.ppat.1010138

Romano, J. D., Nolan, S. J., Porter, C., Ehrenman, K., Hartman, E. J., Hsia, R. and Coppens, I. (2017). The parasite *Toxoplasma* sequesters diverse Rab host vesicles within an intravacuolar network. *J. Cell Biol.* **216**, 4235-4254. doi:10.1083/jcb.201701108

Romano, J. D., Hartman, E. J. and Coppens, I. (2021). Quantitative fluorescence microscopy for detecting mammalian rab vesicles within the parasitophorous vacuole (PV) of the human pathogen *Toxoplasma gondii*. In *Rab GTPases: Methods and Protocols* (ed. G. Li and N. Segev), pp. 295-305. New York, NY: Springer US.

Roos, D. S., Donald, R. G., Morrissette, N. S. and Moulton, A. L. (1994). Molecular tools for genetic dissection of the protozoan parasite *Toxoplasma gondii*. *Methods Cell Biol.* **45**, 27-63. doi:10.1016/S0091-679X(08)61845-2

Schöneberg, J., Lee, I.-H., Iwasa, J. H. and Hurley, J. H. (2017). Reverse-topology membrane scission by the ESCRT complexes. *Nat. Rev. Mol. Cell Biol.* **18**, 5-17. doi:10.1038/nrm.2016.121

Sibley, L. D., Niesman, I. R., Parmley, S. F. and Cesbron-Delauw, M. F. (1995). Regulated secretion of multi-lamellar vesicles leads to formation of a tubulo-vesicular network in host-cell vacuoles occupied by *Toxoplasma gondii*. *J. Cell Sci.* **108**, 1669-1677. doi:10.1242/jcs.108.4.1669

Sinai, A. P., Webster, P. and Joiner, K. A. (1997). Association of host cell endoplasmic reticulum and mitochondria with the *Toxoplasma gondii* parasitophorous vacuole membrane: a high affinity interaction. *J. Cell Sci.* **110**, 2117-2128. doi:10.1242/jcs.110.17.2117

Sun, S., Zhou, X., Corvera, J., Gallick, G. E., Lin, S.-H. and Kuang, J. (2015). ALG-2 activates the MVB sorting function of ALIX through relieving its intramolecular interaction. *Cell Discov.* **1**, 15018. doi:10.1038/celldisc.2015.18

Tang, S., Henne, W. M., Borbat, P. P., Buchkovich, N. J., Freed, J. H., Mao, Y., Fromme, J. C. and Emr, S. D. (2015). Structural basis for activation, assembly and membrane binding of ESCRT-III Snf7 filaments. *Elife* **4**, e12548. doi:10.7554/eLife.12548

Teis, D., Saksena, S. and Emr, S. D. (2008). Ordered assembly of the ESCRT-III complex on endosomes is required to sequester cargo during MVB formation. *Dev. Cell* **15**, 578-589. doi:10.1016/j.devcel.2008.08.013

Vietri, M., Radulovic, M. and Stenmark, H. (2020). The many functions of ESCRTs. *Nat. Rev. Mol. Cell Biol.* **21**, 25-42. doi:10.1038/s41580-019-0177-4

Von Schwedler, U. K., Stuchell, M., Müller, B., Ward, D. M., Chung, H.-Y., Morita, E., Wang, H. E., Davis, T., He, G.-P., Cimbora, D. M. et al. (2003). The protein network of HIV budding. *Cell* **114**, 701-713. doi:10.1016/S0092-8674(03)00714-1

Yang, B., Stjepanovic, G., Shen, Q., Martin, A. and Hurley, J. H. (2015). Vps4 disassembles an ESCRT-III filament by global unfolding and processive translocation. *Nat. Struct. Mol. Biol.* **22**, 492-498. doi:10.1038/nsmb.3015